The Hsp90 cochaperone TTT promotes cotranslational maturation of PIKKs prior to complex assembly

Damien Toullec, Alberto Elías-Villalobos, Céline Faux, Ambre Noly, Gwendaline Lledo, Martial Séveno, Dominique Helmlinger

Cell Reports

Article

The Hsp90 cochaperone TTT promotes cotranslational maturation of PIKKs prior to complex assembly

Graphical abstract

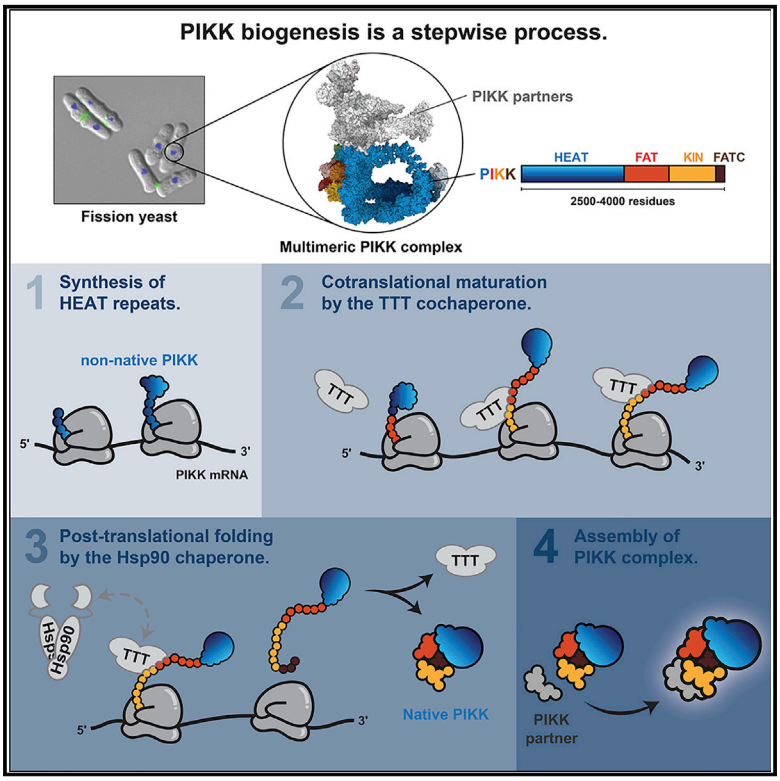

Highlights

- The Hsp90 cochaperone TTT recognizes PIKKs cotranslationally
- TTT binds to the structurally related FATKIN unit
- Nascent PIKKs remain in a non-native state until translation is completed
- The cotranslational maturation of PIKKs precedes their assembly into larger complexes

Authors

Damien Toullec, Alberto Elías-Villalobos, Céline Faux, Ambre Noly, Gwendaline Lledo, Martial Séveno, Dominique Helmlinger

Correspondence

dhelmlinger@crbm.cnrs.fr

In brief

Toullec et al. explore the assembly of PIKK complexes as a paradigm to understand the principles governing the biogenesis of multimeric complexes. Biochemical and functional analyses show that, in fission yeast, PIKK maturation and assembly occur sequentially, rather than simultaneously, and require distinct factors and mechanisms.

Toullec et al., 2021, Cell Reports 37, 109867
October 19, 2021
https://doi.org/10.1016/j.celrep.2021.109867

CellPress

Cell Reports

CellPress
OPEN ACCESS

Article

The Hsp90 cochaperone TTT promotes cotranslational maturation of PIKKs prior to complex assembly

Damien Toullec,[1,3] Alberto Elías-Villalobos,[1,3,4] Céline Faux,[1] Ambre Noly,[1] Gwendaline Lledo,[1] Martial Séveno,[2] and Dominique Helmlinger[1,5,*]

[1]CRBM, University of Montpellier, CNRS, Montpellier, France
[2]BioCampus Montpellier, University of Montpellier, CNRS, INSERM, Montpellier, France
[3]These authors contributed equally
[4]Present address: Institut Curie, UMR3244, Paris, France
[5]Lead contact
*Correspondence: dhelmlinger@crbm.cnrs.fr
https://doi.org/10.1016/j.celrep.2021.109867

SUMMARY

Phosphatidylinositol 3-kinase-related kinases (PIKKs) are a family of kinases that control fundamental processes, including cell growth, DNA damage repair, and gene expression. Although their regulation and activities are well characterized, little is known about how PIKKs fold and assemble into active complexes. Previous work has identified a heat shock protein 90 (Hsp90) cochaperone, the TTT complex, that specifically stabilizes PIKKs. Here, we describe a mechanism by which TTT promotes their *de novo* maturation in fission yeast. We show that TTT recognizes newly synthesized PIKKs during translation. Although PIKKs form multimeric complexes, we find that they do not engage in cotranslational assembly with their partners. Rather, our findings suggest a model by which TTT protects nascent PIKK polypeptides from misfolding and degradation because PIKKs acquire their native state after translation is terminated. Thus, PIKK maturation and assembly are temporally segregated, suggesting that the biogenesis of large complexes requires both dedicated chaperones and cotranslational interactions between subunits.

INTRODUCTION

Most proteins function as part of multimeric complexes rather than in isolation. These complexes adopt specific quaternary structures that are important for their functions, for example, enabling allosteric regulation. Describing the principles that govern their assembly is key to understanding their organization, function, and regulation. Pioneering work revealed that complexes assemble through ordered pathways that appear evolutionarily conserved (Marsh et al., 2013). However, compared with our knowledge of the structure, biochemical composition, and regulatory activities of protein complexes, less is known about the mechanisms and factors controlling their biogenesis.

Two distinct mechanisms promote assembly while minimizing misfolding and non-specific interactions, thereby preventing proteotoxic stress (Marsh and Teichmann, 2015). First, both pleiotropic and dedicated chaperones assist the folding of newly synthesized subunits and promote protein-protein interactions, sometimes at specific organelles (Kramer et al., 2019). Second, cotranslational interactions between subunits of the same complex recently emerged as a mechanism driving protein maturation (Natan et al., 2017). Various proteins can indeed recognize the nascent polypeptide of their interacting partner in prokaryotes and eukaryotes, indicating a general phenomenon (Duncan and Mata, 2011; Shiber et al., 2018; Shieh et al., 2015). These mechanisms might be mutually exclusive, because subunits that do not engage cotranslationally require specific chaperones for their assembly (Shiber et al., 2018). However, which features dictate whether a nascent polypeptide requires its partner or dedicated assembly factors for folding and maturation are not well understood. Moreover, whether both mechanisms cooperate to drive the biogenesis of certain complexes is unclear.

These studies typically focused on complexes with relatively simple architecture and formed by a small number of subunits. Comparatively less is known about the assembly of large complexes containing multiple distinct modules. Their biogenesis may follow an ordered pathway, with each step involving a distinct mechanism. For example, proteasome assembly requires both concerted action of dedicated chaperones and cotranslational interactions between specific subunits (Funakoshi et al., 2009; Panasenko et al., 2019; Roelofs et al., 2009; Saeki et al., 2009). Similarly, although less characterized, the assembly of transcription complexes involves both mechanisms. Cotranslational interactions have been observed between some subunits of the SET1C histone methyltransferase, the general transcription factor TFIID, or the SAGA coactivator (Halbach et al., 2009; Kamenova et al., 2019; Kassem et al., 2017). In contrast, both the TFIID-specific subunit TAF5 and its SAGA-specific

paralog TAF5L require the CCT chaperonin for their incorporation into pre-assembled modules (Antonova et al., 2018). Likewise, we recently showed that assembly of the Tra1/TRRAP subunit into the SAGA and NuA4/TIP60 transcription complexes requires a dedicated assembly factor, called the Triple T complex (TTT) (Detilleux et al., 2021; Elías-Villalobos et al., 2019a).

Yeast Tra1 and its human ortholog TRRAP are evolutionarily conserved members of the family of phosphatidylinositol 3-kinase (PI3K)-related kinases (PIKKs) (McMahon et al., 1998; Saleh et al., 1998; Vassilev et al., 1998). However, Tra1/TRRAP lacks the residues required for catalytic activity and is the only pseudokinase of this family. Tra1/TRRAP functions as a large protein interaction hub and is essential for the activity of many transcription factors. Active PIKKs function as serine/threonine kinases, mediating signal transduction in diverse biological contexts (Lempiäinen and Halazonetis, 2009). DNA-PK, ATM, and ATR have essential roles in DNA damage sensing, signaling, and repair. MTOR is a central regulator of metabolism, cell growth, and survival in response to nutrients and growth factors. Finally, SMG1 mediates the decay of mRNAs with premature stop codons or splicing defects. Although PIKKs are generally conserved across eukaryotic clades, yeasts lack orthologs of DNA-PK and SMG1 (Elías-Villalobos et al., 2019b). Despite these diverse functions, PIKKs share a characteristic domain architecture and are structurally related (Imseng et al., 2018). A long stretch of Huntingtin, EF3A, ATM, TOR (HEAT) repeats precedes the FRAP, ATM and TRRAP (FAT) domain, which consists of tetratricopeptide (TPR) repeats, followed by the kinase (KIN) domain. Both HEAT and TPR repeats form extended arrays of α-solenoidal repeats that fold into extended superhelical structures. Topologically, the FAT domain forms a single FATKIN unit with the KIN domain and the PIKK regulatory domain (PRD). Its C-terminal (C-ter) end, the FATC motif, is composed of short, hydrophobic α-helices buried inside the structure, close to the activation loop. The FATKIN unit is highly conserved and has a similar architecture between PIKKs (Imseng et al., 2018). In contrast, the N-terminal (N-ter) HEAT repeats are more variable, both in length and in topology. In addition, both ATM and ATR lack the FKBP-rapamycin-binding (FRB) domain, a short region between the FAT and the KIN domains. PIKKs also differ in their oligomerization and interaction with regulatory factors. For example, MTOR dimerizes constitutively and interacts with specific partners to form either TORC1 or TORC2 complexes. Tra1/TRRAP is always monomeric but part of larger complexes, the SAGA and NuA4/TIP60 transcription coactivators.

The biogenesis of PIKK complexes remained uncharacterized for many years, until seminal work revealed that PIKKs share a dedicated heat shock protein 90 (Hsp90) cochaperone, the TTT complex, for their maturation and *de novo* assembly (Anderson et al., 2008; Hurov et al., 2010; Izumi et al., 2012; Kaizuka et al., 2010; Takai et al., 2007, 2010). TTT was initially discovered in *Schizosaccharomyces pombe* and is composed of three conserved, specific subunits: Tel2, Tti1, and Tti2 (Hayashi et al., 2007; Shevchenko et al., 2008; Takai et al., 2010). Functional studies performed mostly in yeast and mammalian cells implicated TTT in PIKK signaling pathways, for example, in response to DNA damage or metabolic stress (Ahmed et al., 2001; Anderson et al., 2008; Brown and Gromeier, 2017; David-Morrison et al., 2016; Goto et al., 2017; Hoffman et al., 2016; Hurov et al., 2010; Izumi et al., 2012; Kaizuka et al., 2010; Kim et al., 2013; Rao et al., 2014; Shikata et al., 2007; Takai et al., 2007; Xu et al., 2019). Although catalytically inactive, Tra1/TRRAP stability, complex assembly, and transcriptional activity also require TTT and Hsp90 (Detilleux et al., 2021; Elías-Villalobos et al., 2019a; Hurov et al., 2010; Izumi et al., 2012; Kaizuka et al., 2010; Takai et al., 2007). However, the molecular mechanism by which TTT recognizes PIKKs specifically and promotes their maturation is not known. Here, using *S. pombe*, we show that TTT interacts with PIKKs cotranslationally and recognizes nascent PIKK polypeptides in a non-native state until synthesis is completed.

RESULTS

Proteomic characterization of the *S. pombe* TTT cochaperone

Fission yeast offers several advantages to study how the Hsp90 cochaperone TTT regulates PIKK biogenesis. Its genome has six genes, each encoding a PIKK present only in one complex (Figure 1A). In *Saccharomyces cerevisiae* and mammals, Tra1/TRRAP is shared between the SAGA and the NuA4/TIP60 complexes. In contrast, *S. pombe* has two paralogs, Tra1 and Tra2, which have non-redundant roles that are specific for SAGA and NuA4, respectively (Helmlinger et al., 2011). Similarly, MTOR has two paralogs, Tor2 and Tor1, which incorporate into the TORC1 and TORC2 complexes, respectively (Hayashi et al., 2007). Finally, Rad3 is the *S. pombe* ortholog of Mec1/ATR, which interacts with the Ddc2/ATRIP ortholog Rad26, and Tel1 is the ortholog of Tel1/ATM, which interacts with the MRN complex (Blackford and Jackson, 2017).

We first performed an unbiased proteomic characterization of TTT in *S. pombe*, using tandem affinity purification of endogenous Tel2, Tti1, and Tti2 followed by quantitative mass spectrometry (TAP-MS). Consistent with previous studies (Hayashi et al., 2007; Takai et al., 2010), Tti2 interacts with Tel2 and Tti1 almost stoichiometrically (Figures 1B and S1A; Table S1). Interestingly, Tti2 also pulls down Asa1, a protein previously identified in Rvb1 purifications from both *S. cerevisiae* and *S. pombe* (Shevchenko et al., 2008) and involved in PIKK stability (Goto et al., 2017; Rozario and Siede, 2012; Stirling et al., 2011). In contrast, the AAA+ ATPases Rvb1 and Rvb2 were detected with poorer specificity and reproducibility, suggesting weaker or more transient interaction with Tti2. The Hsp90 chaperone was not specifically detected in Tti2 purifications, possibly because of its high abundance in protein extracts. Similar observations were made in quantitative mass spectrometry (MS) analyses of Tel2 and Tti1 purifications (Figure S1A; Table S2).

In addition, most PIKKs were specifically and reproducibly enriched in Tti2, Tel2, and Tti1 purifications, including Tra1, Tra2, Tor2, and Tor1 (Figures 1B and S1A; Table S2). We observed no and weak interaction with Tel1 and Rad3, respectively, possibly because of their low abundance and negligible DNA damage in exponentially growing cells. We found no detectable interaction between TTT and subunits from PIKK-containing complexes, such as SAGA, NuA4, TORC1, and TORC2. One notable exception is Wat1, a subunit shared between the TORC1 and the

CellPress
OPEN ACCESS

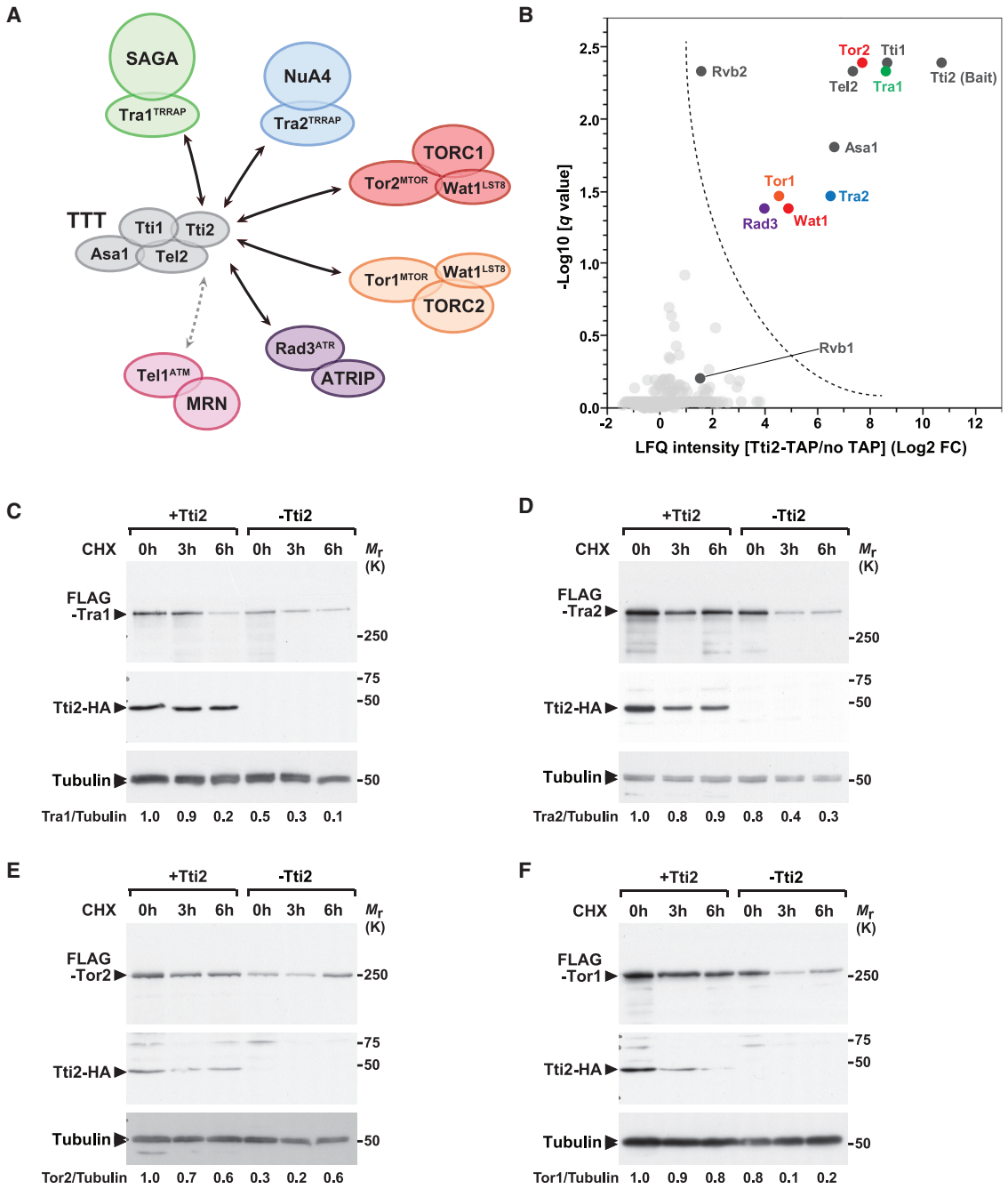

Figure 1. TTT interacts with PIKKs and promotes their stability

(A) Illustration of TTT complex components (gray) and the interacting PIKK substrates, shown within their complexes. Shown are *S. pombe* names with human orthologs in superscript.

(B) Mass spectrometry analysis (LC-MS/MS) of tandem affinity-purified Tti2. Volcano plot showing the average ratios of label-free quantification (LFQ) intensities in Tti2-TAP over control "no TAP" purifications against normalized p values (q) (n = 4). Each dot represents one protein, colored as in (A).

(C–F) PIKK steady-state levels and stability upon conditional deletion of *tti2+*. *tti2-CKO* strains in which endogenous Tra1 (C), Tra2 (D), Tor2 (E), and Tor1 (F) are FLAG-tagged were grown to the exponential phase, treated with either DMSO (+Tti2) or β-estradiol (−Tti2) for 20 h, and then treated with 100 μM cycloheximide (CHX) for 3 and 6 h before harvesting. Western blots of protein extracts were probed with anti-FLAG, anti-HA, and anti-tubulin antibodies. Numbers below show the mean signal intensity for each PIKK, normalized to tubulin (n = 2).

TORC2 complexes, which interacts with all three TTT components. Altogether, our quantitative proteomic analyses indicate that Tti2, Tel2, and Tti1, together with Asa1, form a stable multimeric complex that interacts with most PIKKs in *S. pombe* (Figure 1A).

TTT regulates PIKK functions

We next examined the effect of TTT on PIKK-dependent processes. As shown in other organisms, Tel2, Tti1, and Tti2 are essential for viability in *S. pombe* (Inoue et al., 2017; Shikata et al., 2007). We thus constructed strains in which TTT subunits can be conditionally depleted. We first used the auxin-inducible degron (AID), which allows rapid depletion and has been successfully implemented in *S. pombe* (Kanke et al., 2011; Nishimura et al., 2009). Western blot analyses of endogenous AID-tagged Tel2, Tti1, and Tti2 shows auxin-dependent depletion in TIR1-expressing strains, although Tti2 appears partially destabilized even without auxin (Figure S1B). Depletion of each protein reduces *S. pombe* viability and proliferation compared with control strains and culture conditions (Figures S1C and S1D).

Previous work demonstrated that TTT is required for activation of the DNA replication checkpoint by Rad3 (Shikata et al., 2007; Xu et al., 2019). We thus characterized the contribution of TTT to the functions of other PIKKs, particularly Tra1 and Tor2. Both have crucial roles in the switch between proliferation and sexual differentiation in *S. pombe* as part of the SAGA and TORC1 complexes, respectively (Laribee, 2018). We used qRT-PCR to determine the effect of TTT depletion on the expression of two sexual differentiation genes, *ste11+* and *mei2+*. We observed that the mRNA levels of both genes increase upon depletion of Tel2, Tti1, and Tti2 compared with control strains and conditions (Figures S1E and S1F). This phenotype is reminiscent of that observed in the absence of Tra1 or upon partial inactivation of Tor2 (Alvarez and Moreno, 2006; Helmlinger et al., 2011). Therefore, similar to Tra1 and Tor2, TTT represses sexual differentiation genes in nutrient-rich conditions. Finally, we examined TORC1 activity in TTT-depleted cells. Western blotting showed decreased phosphorylation of the ribosomal protein S6, a canonical TORC1 substrate, following Tel2, Tti1, and Tti2 depletion (Figure S1G). We conclude that the TTT complex promotes proliferation and inhibits sexual differentiation when nutrients are present, presumably by incorporating Tra1 and Tor2 into SAGA and TORC1, respectively.

TTT promotes PIKK stability

Genetic and biochemical studies established that TTT sustains PIKK steady-state levels in yeast, mouse, and human cell lines (Anderson et al., 2008; Fernández-Sáiz et al., 2013; Genereaux et al., 2012; Goto et al., 2017; Hoffman et al., 2016; Hořejší et al., 2010; Hurov et al., 2010; Izumi et al., 2012; Kaizuka et al., 2010; Rao et al., 2014; Rozario and Siede, 2012; Stirling et al., 2011; Takai et al., 2007, 2010; Xu et al., 2019). Surprisingly, we found that auxin-induced depletion of Tel2, Tti1, and Tti2 had no detectable effect on PIKK protein levels in *S. pombe*. However, AID targeting of TTT subunits causes incomplete depletion and partial growth defects, even after prolonged auxin treatment (Figures S1B–S1D). We thus switched to a conditional gene deletion strategy, based on inducible CreER-loxP-mediated recombination. We previously generated and characterized a conditional knockout allele of *tti2+* (*tti2-CKO*), which allows complete, β-estradiol-induced loss of Tti2 (Elías-Villalobos et al., 2019a). To measure the effect of TTT on both PIKK steady-state levels and stability, we performed a cycloheximide (CHX) chase using different *tti2-CKO* strains in which endogenous PIKKs were FLAG-tagged at their N-ter end. Western blotting followed by quantification of signal intensities showed that both the steady-state levels and the stability of Tra1, Tra2, and Tor1 decrease following Tti2 depletion (Figures 1C–1F). Surprisingly, despite a strong decrease of Tor2 steady-state levels, its stability appears unaffected, even increasing 6 h after CHX treatment. It is possible that Tor2 is subjected to rapid turnover and compensatory mechanisms boosting its synthesis. Indeed, *S. pombe* can resist CHX and continue to grow, although more slowly. Despite several attempts, we were unable to reproducibly detect endogenous Rad3 and Tel1, precluding analysis of their expression by this approach. However, a study isolated a *tel2* mutation that destabilizes the TTT complex and reduces Rad3 and Tel1 protein levels in *S. pombe* (Xu et al., 2019). Finally, our published transcriptomic analysis of *tti2-CKO* mutants showed that PIKK mRNA levels remain unaffected following Tti2 depletion (Figure S1H) (Elías-Villalobos et al., 2019a), indicating that TTT regulates their expression at the protein level. In conclusion, together with previous work (Shikata et al., 2007; Xu et al., 2019), our results show that in *S. pombe*, the TTT cochaperone promotes the stability of PIKKs and contributes to their regulatory roles. This function of TTT is therefore conserved among budding yeast, fission yeast, and mammals.

TTT binds to PIKKs cotranslationally

We then sought to determine where TTT recognizes PIKKs within the cell. We recently showed that TTT promotes Tra1 and Tra2 incorporation into SAGA and NuA4, respectively, and contributes to their gene regulatory activities (Elías-Villalobos et al., 2019a). However, chromatin immunoprecipitation (ChIP) revealed no enrichment of Tel2 over background at SAGA-bound (*mei2+*) and NuA4-bound (*ssa2+*) promoters (Figure S2A), suggesting that TTT does not control Tra1 and Tra2 assembly at promoters. Furthermore, fluorescent live microscopy showed that endogenous GFP-tagged Tel2 does not localize to the nucleus in standard growth conditions (Figure S2B). We thus hypothesized that rather than acting at chromatin, TTT recognizes newly synthesized Tra1 and Tra2.

To test this possibility, we performed RNA immunoprecipitation (RIP) of TTT. Previous work has shown that RIP can detect cotranslational interactions between a protein and a nascent polypeptide (Duncan and Mata, 2011, 2014). Conventional and qRT-PCR analyses revealed a specific enrichment of the *tra1*$^{+}$ mRNA in RIPs of all three TTT subunits, Tel2, Tti1, and Tti2, compared with several negative controls (Figures 2A and 2B). These include a non-reverse transcribed (no RT) control, a strain lacking the epitope tag used to purify TTT (no hemagglutinin [HA]), and a strain in which the HA tag was fused to the TORC2 subunit Ste20, which does not interact with Tra1 and SAGA. In addition, we measured the binding of TTT to mRNAs encoding proteins unrelated to PIKK biogenesis and function. Specifically, we tested the vacuolar serine protease Isp6, the glutathione S-transferase

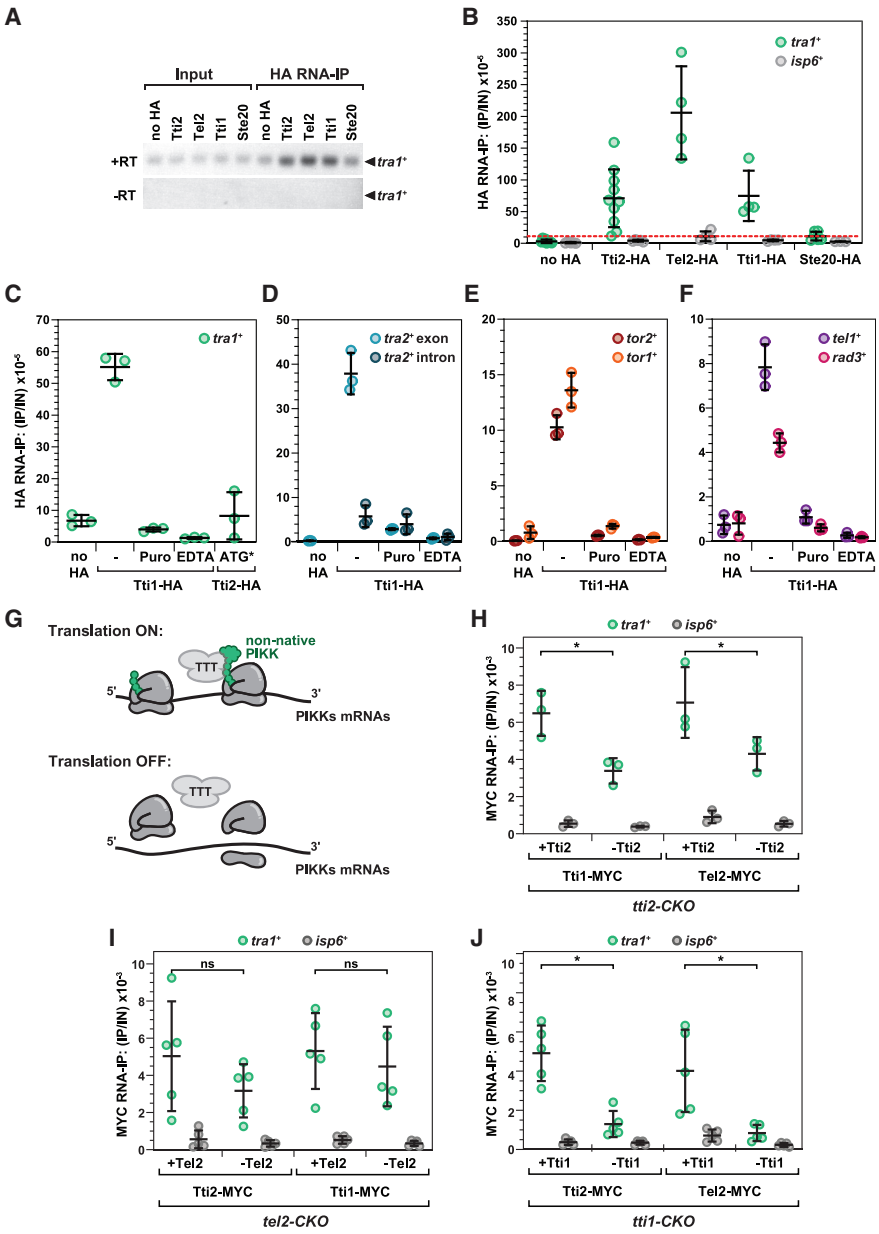

Figure 2. TTT recognizes PIKKs cotranslationally through Tti1 and Tti2

RNA immunoprecipitation of TTT subunits followed by qRT-PCR analyses (RIP-qPCR). Immunoprecipitation (IP) using anti-HA (A–F) and anti-MYC (H–J) antibodies from exponentially growing cells (A–F) and treated with either DMSO or β-estradiol for 16 h (H–J). Ratios of IP to input (IP/IN) from independent experiments are shown as individual points ($n \geq 3$) overlaid with the mean and standard deviation (SD). The *isp6*+ mRNA is used as the negative control. An untagged strain is used as a control for the background IP signal. (C–F) For translation inhibition, cultures were treated with 1 mg/mL puromycin for 15 min. For ribosome dissociation, total extracts were supplemented with 25 mM EDTA.

(A) RT-PCR profile of *tra1*+ mRNAs in Tel2-HA, Tti1-HA, and Tti2-HA RIPs.

(B) qPCR analysis of *tra1*+ mRNA levels in Tel2-HA, Tti1-HA, and Tti2-HA RIPs. The red dashed line indicates an unspecific background signal.

(C) *tra1*+ and *tra1-ATG** levels in Tti1-HA RIPs. The ATG start codon is mutated to TAA in the *tra1-ATG** strain.

(D) *tra2*+ levels in Tti1-HA RIPs, quantified using primers amplifying either an exon or an intron.

(E) *tor1*+ and *tor2*+ levels in Tti1-HA RIPs.

(F) *tel1*+ and *rad3*+ levels in Tti1-HA RIPs.

(G) Model of TTT binding to newly synthetized PIKK polypeptides during translation.

(H) *tra1*+ levels in Tti1-MYC and Tel2-MYC RIPs upon *tti2*+ deletion (*tti2-CKO*).

(I) *tra1*+ levels in Tti2-MYC and Tti1-MYC RIPs upon *tel2*+ deletion (*tel2-CKO*).

(J) *tra1*+ levels in Tti2-MYC and Tel2-MYC RIPs upon *tti1*+ deletion (*tti1-CKO*).

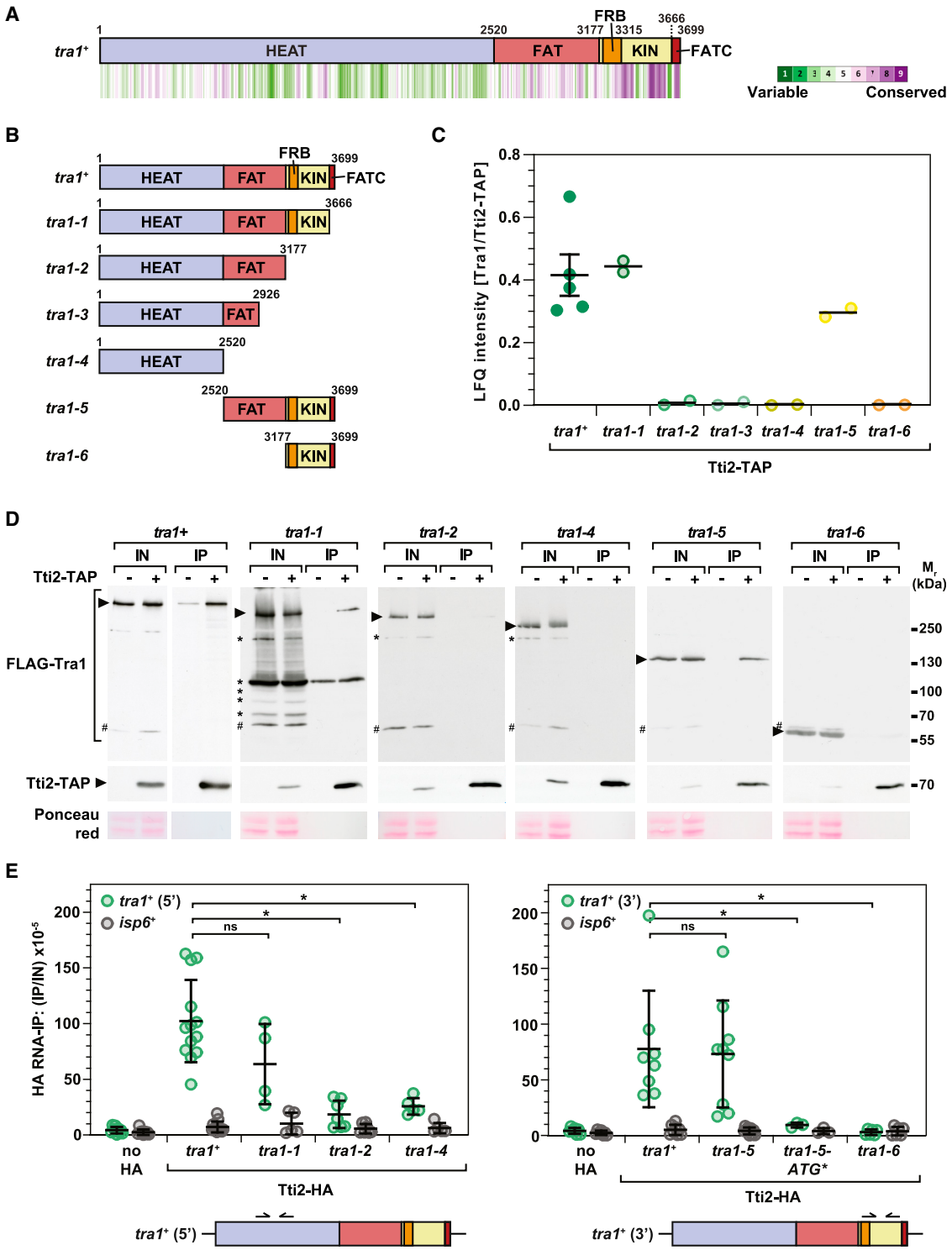

Figure 3. The FATKIN unit of Tra1 mediates its binding to TTT

(A) Evolutionary conservation analysis of *S. pombe* PIKKs. Conservation scores were calculated using ConSurf (Ashkenazy et al., 2016) from multiple sequence alignments generated using Clustal Omega (Madeira et al., 2019). Scores were averaged in 25-residue bins, shown as a heatmap (see the color scale), and aligned to Tra1 domains (HEAT, FAT, FRB, KIN, and FATC).

(B) Illustration of *S. pombe* Tra1 truncations, which remove the FATC domain (*tra1-1*); the KIN and FATC domains (*tra1-2*); half of the FAT, KIN, and FATC domains (*tra1-3*); the entire FAT, KIN, and FATC domains (*tra1-4*); the HEAT repeats (*tra1-5*); or the HEAT and FAT domains (*tra1-6*). The first and last residues of each truncated mutant are shown.

(legend continued on next page)

Gst2, and the cell-surface endo-1,3-beta-glucanase Eng1. Compared with control purifications, we found no enrichment of the *isp6*$^+$, *gst2*$^+$, and *eng1*$^+$ mRNAs in Tti2, Tel2, and Tti1 RIPs (Figures 2B and S2C), confirming the specificity of the interaction between TTT and *tra1*$^+$.

To determine whether this interaction occurs cotranslationally, we then repeated Tti1 RIPs in cells treated either with puromycin, an inhibitor of translation elongation, or with EDTA, which dissociates ribosomes. Both treatments abolished Tti1 binding to *tra1*$^+$ (Figure 2C). Likewise, mutating the *tra1* ATG start codon to TAA reduced the binding of Tti2 to background levels (Figure 2C). Next, we observed comparable enrichment of *tra2*$^+$, *tor2*$^+$, and *tor1*$^+$, and to a lesser extent *rad3*$^+$ and *tel1*$^+$, in Tti1 RIPs (Figures 2D–2F). Tti1 binding to all mRNAs decreases to background levels following translation inhibition and ribosome dissociation, using puromycin and EDTA, respectively. We verified that our brief puromycin treatment does not affect Tti1 protein levels (Figure S2D). Finally, the presence of an intron within *tra2*$^+$ allowed us to confirm that Tti1 binds the mature isoform of *tra2*$^+$, but not its pre-mRNA (Figure 2D). Altogether, these observations indicate that TTT binds all PIKK-encoding mRNAs in *S. pombe*. This interaction most likely occurs indirectly, because TTT subunits do not have predicted RNA-binding motifs. Furthermore, TTT requires active and intact ribosomes to bind these mRNAs, indicating that TTT recognizes nascent PIKK polypeptides during their translation (Figure 2G).

Tti1 and Tti2 contribute to TTT cotranslational binding to PIKKs

We next asked which TTT subunit mediates its interaction with PIKKs by repeating these experiments in conditional deletion mutants of Tti2, Tel2, and Tti1. Similar to the strategy used to obtain the *tti2-CKO* strain, we constructed *tel2-CKO* and *tti1-CKO* mutants in which *tel2*$^+$ and *tti1*$^+$, respectively, can be conditionally deleted upon inducible CreER-loxP-mediated recombination (Figures S3A–S3D). Both strains showed β-estradiol-induced loss of Tel2 and Tti1, which correlated with progressive proliferation defects, whereas no obvious decrease in viability was observed within the time frame analyzed (Figures S3E–S3I). We then backcrossed each mutant with strains in which Tti2, Tel2, or Tti1 was tagged with a MYC epitope. Western blotting showed that the steady-state levels of each subunit remained unaffected by the loss of the two other components (Figures S3I–S3K), allowing TTT purifications.

We next performed RIPs of each TTT subunit in the *tti2-*, *tel2-*, and *tti1-CKO* strains, followed by qRT-PCR analysis of the *tra1*$^+$ mRNA a proxy for the other PIKKs. We observed about a two-fold reduction of Tti1 and Tel2 binding upon Tti2 depletion (Figure 2H). In contrast, Tti2 and Tti1 interaction with *tra1*$^+$ does not change in the absence of Tel2 (Figure 2I), whereas loss of Tti1 caused a strong decrease of Tti2 and Tel2 binding (Figure 2J). We conclude that Tti1, and to a lesser extent Tti2, recruits TTT to nascent Tra1 polypeptides. Even without Tti1, the *tra1*$^+$ mRNA remains detectable in TTT RIPs compared with *isp6*$^+$. This residual binding may involve Tti2 or other factors, such as Asa1.

The FATKIN unit of Tra1 mediates its cotranslational interaction with TTT

To understand how TTT recognizes PIKKs, we performed a structure-function analysis of their interaction. For this, we focused on Tra1 and Tor1 for two reasons. First, Tel1 and Rad3 interact weakly with TTT in normal growth conditions (Figure 1). Second, both Tra2 and Tor2 are essential for viability, complicating genetic analyses (Helmlinger et al., 2011; Weisman and Choder, 2001). Indeed, we wanted to construct endogenous truncation mutants and measure their interaction with TTT *in vivo*. We reasoned that using recombinant fragments may not recapitulate the binding of TTT to nascent polypeptides.

PIKKs are large proteins, ranging from 2,335 residues for Tor1 to 3,661 residues for Tra1 in *S. pombe*. We first constructed a series of mutants that sequentially shorten Tra1 from either its C-ter or its N-ter end (Figures 3A and 3B) and quantified their interaction with TTT using quantitative TAP-MS (Figure 3C). Analysis of the *tra1-2*, *tra1-3*, and *tra1-4* mutants showed that Tra1 does not interact with Tti2 when either the KIN domain, including the FRB region, or larger portions of the FAT and KIN domains are deleted. In contrast, analysis of the *tra1-1* mutant showed that removing the FATC region does not affect Tra1 interaction with Tti2. Similarly, the Tra1-5 mutant, which lacks the long N-ter HEAT repeats, still interacts with Tti2. These observations suggest that the HEAT repeats are not required for Tti2 binding to Tra1, whereas the FATKIN unit is both necessary and sufficient. However, comparing the *tra1-2* with the *tra1-6* mutant showed that Tti2 does not recognize the KIN domain alone, although it is required for the interaction.

One caveat from these TAP-MS quantifications is the absence of normalization to the amount of each mutant protein in the extract. This issue is important because truncated proteins might be unstable. We thus verified that all mutants are expressed at comparable levels using western blotting of total extracts from strains with each *tra1* mutant FLAG-tagged at its N-ter end (Figure 3D). In addition, we used these strains to perform coimmunoprecipitation (coIP) and, overall, confirmed the results obtained by quantitative MS. We observed no detectable interaction between Tti2 and Tra1 truncation mutants missing either a portion

(C) LC-MS/MS analysis of Tti2 purified from WT and *tra1* mutants. LFQ ratios of Tra1 to Tti2 from at least two independent experiments ($n \geq 2$) are plotted individually with the mean.

(D) CoIPs of FLAG-Tra1 and Tti2-TAP using WT and isogenic truncation mutant strains. An untagged strain is used as a control for the background IP signal. Western blots of IPs and inputs were probed with anti-FLAG and anti-TAP antibodies. Ponceau red served as loading control for the inputs. # labels an unspecific anti-FLAG band in *S. pombe*. * labels Tra1 degradation products. Data are representative of two independent experiments ($n = 2$).

(E) RIP-qPCR of *tra1*$^+$ in Tti2-HA purified from WT and *tra1* mutant strains, analyzed as described in Figure 2. The ATG start codon is mutated to TAA in the *tra1-5-ATG** strain. IP/IN ratios from independent experiments are shown as individual points ($n \geq 3$) overlaid with the mean and SD. The bottom diagram shows the position of the primers used for *tra1+* qPCR. Statistical significance was determined by one-way ANOVA followed by Tukey's multiple comparison tests (*$p < 0.05$).

or the entire FATKIN unit (Figure 3D). In contrast, Tti2 interacts with a mutant lacking the HEAT repeats, similar to full-length Tra1. These coIPs also confirmed that the FATKIN unit binds to Tti2, whereas the KIN domain alone does not. Contrasting with the MS results, quantification of western blot signal intensities revealed a two-fold decrease Tti2 interaction with the FATC truncation mutant, Tra1-1 (*tra1-1*) (Table S3). This discrepancy might result from the lack of normalization of TAP-MS values to input levels of Tra1-1, which appears proteolytically unstable (Figure 3D), or to differences in quantification and normalization methods between MS and western blotting. Nevertheless, these results indicate that the FAT and KIN domains mediate Tti2 interaction with Tra1.

Finally, we tested whether the FATKIN unit is also important for Tti2 cotranslational binding to Tra1. For this, we measured the interaction between Tti2 and each *tra1* mutant mRNA by performing RIPs in the same strains used for protein-protein interaction experiments. All RIPs were compared with a control mRNA, *isp6*$^{+}$, and a control no-tag purification. qRT-PCR analyses of Tti2 RIPs showed a pattern similar to that observed in TAP-MS and coIPs (Figure 3E). We observed reduced binding of Tti2 to *tra1-2* and *tra1-4* mutants, in which the KIN and FATKIN domains are deleted, respectively (Figure 3E). In contrast, Tti2 interacts with *tra1-1*, although less efficiently than with full-length *tra1+*, as observed in coIPs, suggesting that the FATC region does not have a major contribution to this interaction. Conversely, analysis of the *tra1-5* and *tra1-6* mutants showed that Tti2 interacts with an mRNA fragment encoding the FATKIN unit, whereas the KIN domain alone is not sufficient (Figure 3E). Finally, mutating the starting ATG codon of the *tra1-5* allele abolished its binding to Tti2, confirming that this interaction requires translation of the truncated mRNA. Overall, our structure-function analysis indicates that the FATKIN unit of Tra1 is both necessary and sufficient for interaction with Tti2, whereas the HEAT repeats are dispensable. These findings suggest that Tti2 is recruited to nascent Tra1 polypeptides at a late stage of translation elongation, only as the FATKIN unit emerges from the ribosome.

TTT recognizes other PIKKs through their FATKIN unit

We next tested whether this model applies to Tor1, another PIKK amenable to mutational analysis. Guided by the results obtained for Tra1, we constructed three Tor1 truncation mutants that remove the KIN domain (*tor1-2*), the FAT and the KIN domains (*tor1-4*), or the HEAT repeats, leaving the FATKIN unit intact (*tor1-5*) (Figures S4A and S4B). Each truncation mutant was tagged with a FLAG epitope and analyzed by coIPs using TAP-tagged Tti2 as bait. Western blotting showed that all mutants are expressed at comparable levels (Figure S4C). We found that the Tor1-4 truncation mutant shows no detectable interaction with Tti2 compared with the background signal (Figure S4C). In contrast, the Tor1-5 mutant, which lacks the HEAT repeats, interacts with Tti2 as efficiently as full-length Tor1. Unexpectedly, we detected an interaction between Tti2 and the Tor1-2 mutant as opposed to what we observed with the corresponding Tra1-2 mutant protein, suggesting different roles of the KIN domain. RIPs followed by qRT-PCR analyses of the cotranslational interaction between Tti2 and the *tor1* mutant mRNAs confirmed these results. Specifically, we observed no detectable interaction between Tti2 and *tor1-4*, whereas Tti2 binds to the *tor1-5* mRNA as efficiently as with full-length *tor1*$^{+}$ (Figure S4D), showing the essential role of the FATKIN unit for this interaction. Finally, in agreement with coIPs, Tti2 interacts with *tor1-2*, from which only the KIN domain is absent. Again, this result contrasts with the lack of interaction observed between Tti2 and the analogous *tra1-2* mutant (Figure 3E).

Our results so far indicate that Tti2 recognizes both Tra1 and Tor1 through their FAT and KIN domains, rather than their HEAT repeats. However, Tti2 does not require the Tor1 KIN domain for binding, whereas it requires both the FAT and the KIN domains of Tra1. To explore this apparent discrepancy, we re-examined multiple sequence alignments of *S. pombe* PIKKs and their metazoan orthologs. The Tor1-2 mutant protein contains a stretch of conserved residues that show similarity to the MTOR FRB domain, whereas the Tra1-2 mutant lacks this region (Figures 3B and S4B). We thus constructed the *tor1-3* allele, which removes an additional 165 residues from the Tor1-2 mutant protein to remove the FRB domain entirely (Figures S4B and S4D). RIP-qPCR analysis showed that Tti2 does not interact with *tor1-3*, indicating that Tti2 requires the FRB domain to interact with Tor1.

Finally, we characterized the cotranslational interaction between Tti2 and the Tel1 PIKK, in which the human ortholog ATM does not have an FRB domain inserted between the FAT and the KIN domains. RIP-qPCR analyses showed that compared with *isp6*$^{+}$, Tti2 interacts with a *tel1-2* mutant mRNA lacking the KIN domain, but not with a *tel1-4* mutant in which both the FAT and the KIN domains are removed (Figure S5). Thus, Tti2 requires the KIN domains of both Tra1 and Tor1 for binding, whereas it requires the FAT domain of Tel1, possibly because the latter does not contain an FRB domain. However, even for Tra1, we demonstrated that the FAT domain contributes to this interaction too (Figures 3C–3E). We therefore conclude that the FATKIN unit of PIKKs mediates their cotranslational recognition by TTT. In agreement, the FAT and KIN domains show the highest structural and sequence similarities between PIKKs (Imseng et al., 2018), which we confirmed for *S. pombe* Tra1 and Tor1 (Figures 3A and S4A).

TTT does not interact with PIKK partners

Most PIKKs function as part of large, multimeric complexes. In *S. pombe*, these include SAGA, NuA4, TORC1, and TORC2, which contain Tra1, Tra2, Tor2, and Tor1, respectively (Figure 1A). Previous work in fission yeast and mammalian cells established that TTT is required for *de novo* incorporation of PIKKs (Elías-Villalobos et al., 2019a; Takai et al., 2010). We thus hypothesized that TTT promotes the cotranslational assembly of nascent PIKKs into their complexes. To test this possibility, we used RIPs to measure the cotranslational interaction between TTT and SAGA, NuA4, TORC1, and TORC2 subunits. All RIPs were compared with a control mRNA, *isp6*$^{+}$, and a control no-tag purification. We first probed Tel2 and Tti2 RIPs for the presence of mRNAs encoding Spt20, Taf12, and Ada1, which are either direct or close interactors of Tra1 within SAGA (Elías-Villalobos et al., 2019a; Papai et al., 2020; Wang et al., 2020). qRT-PCR analyses showed that unlike *tra1*$^{+}$, neither Tti2 nor Tel2 interacts with *ada1*$^{+}$, *spt20*$^{+}$, and *taf12*$^{+}$ (Figure 4A). We next tested whether

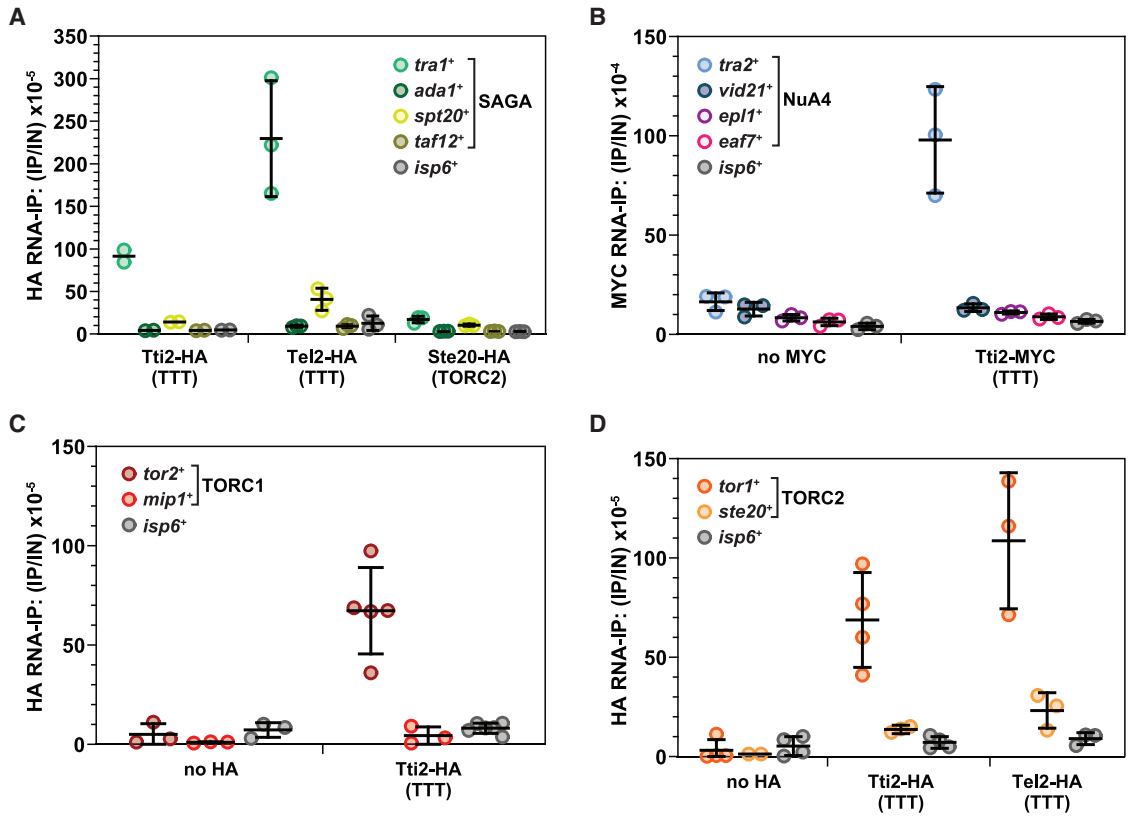

Figure 4. TTT does not interact with PIKK partners

Tel2 and Tti2 RIP-qPCR analyzed as described in Figure 2. IP/IN ratios from independent experiments are shown as individual points ($n \geq 3$) overlaid with the mean and SD.

(A) *tra1+*, *ada1+*, *spt20+*, and *taf12+* levels in Tti2-HA and Tel2-HA IPs.

(B) *tra2+*, *vid21+*, *epl1+*, and *eaf7+* levels in Tti2-MYC IPs.

(C) *tor2+* and *mip1+* levels in Tti2-HA IPs.

(D) *tor1+* and *ste20+* levels in Tti2-HA and Tel2-HA IPs.

TTT interacts with mRNAs encoding the NuA4 subunits Vid21, Epl1, and Eaf7. The *S. cerevisiae* ortholog of Vid21, Eaf1, makes extensive contacts with Tra1 in the NuA4 complex (Wang et al., 2018). We observed no enrichment of *vid21*$^+$, *epl1*$^+$, and *eaf7*$^+$ in Tti2 RIPs, unlike *tra2*$^+$ (Figure 4B). Finally, the TORC1 and TORC2 complexes are each defined by specific subunits that, in *S. pombe*, are the RPTOR ortholog Mip1 and the RICTOR ortholog Ste20, respectively. Again, compared with *tor2*$^+$ and *tor1*$^+$, neither Tti2 nor Tel2 interacts with *mip1*$^+$ and *ste20*$^+$ (Figures 4C and 4D).

In agreement with these findings, we found no evidence of protein-protein interaction between TTT and subunits of SAGA, NuA4, TORC1, or TORC2 in our quantitative TAP-MS analyses, except Wat1 (Table S2). Likewise, in mammals, TELO2 associates with all PIKKs, but not with their partners (Takai et al., 2007, 2010). Conversely, TTT subunits are not detected in affinity purifications of PIKK complexes, such as SAGA or NuA4 (Elías-Villalobos et al., 2019a; Helmlinger et al., 2011). TTT is only detected when the Tra1, Tra2, Tor2, and Tor1 PIKKs are used as baits (Hayashi et al., 2007; Helmlinger et al., 2011; Inoue et al., 2017). Altogether, these observations suggest that PIKKs interact with TTT and their partners in a mutually exclusive manner.

PIKKs do not assemble cotranslationally

Recent work revealed widespread cotranslational assembly of protein complexes (Shiber et al., 2018), including of human and *S. cerevisiae* SAGA subunits (Kamenova et al., 2019; Kassem et al., 2017). We thus determined whether PIKKs can engage in cotranslational interactions with their partners. For this, we performed RIPs of SAGA-, NuA4-, TORC1-, and TORC2-specific subunits and quantified mRNAs encoding the corresponding PIKK. All RIPs were compared with a control mRNA, *isp6*$^+$, and a control no-tag purification. qRT-PCR showed that the *tra1*$^+$ mRNA is not enriched in purifications of the SAGA subunit Taf12 (Figure 5A). Similarly, the NuA4 subunit Mst1 did not copurify with *tra2*$^+$ (Figure 5B). Finally, we found no detectable enrichment of *tor2*$^+$ and *tor1*$^+$ in Mip1 and Ste20 purifications, respectively (Figures 5C and 5D). We included two types of positive controls to strengthen these observations. First, concomitant purifications of Tti2 robustly enriched *tra1*$^+$, *tra2*$^+$, *tor2*$^+$, and *tor1*$^+$, as expected (Figures 5A–5D). Second, the ability of a protein to copurify with its own mRNAs during translation (Duncan and Mata, 2011) allowed us to directly control the efficiency of each RIP. All anti-HA RIPs are performed using strains in which the protein of interest is C-ter-tagged with an HA-TAP fusion, but

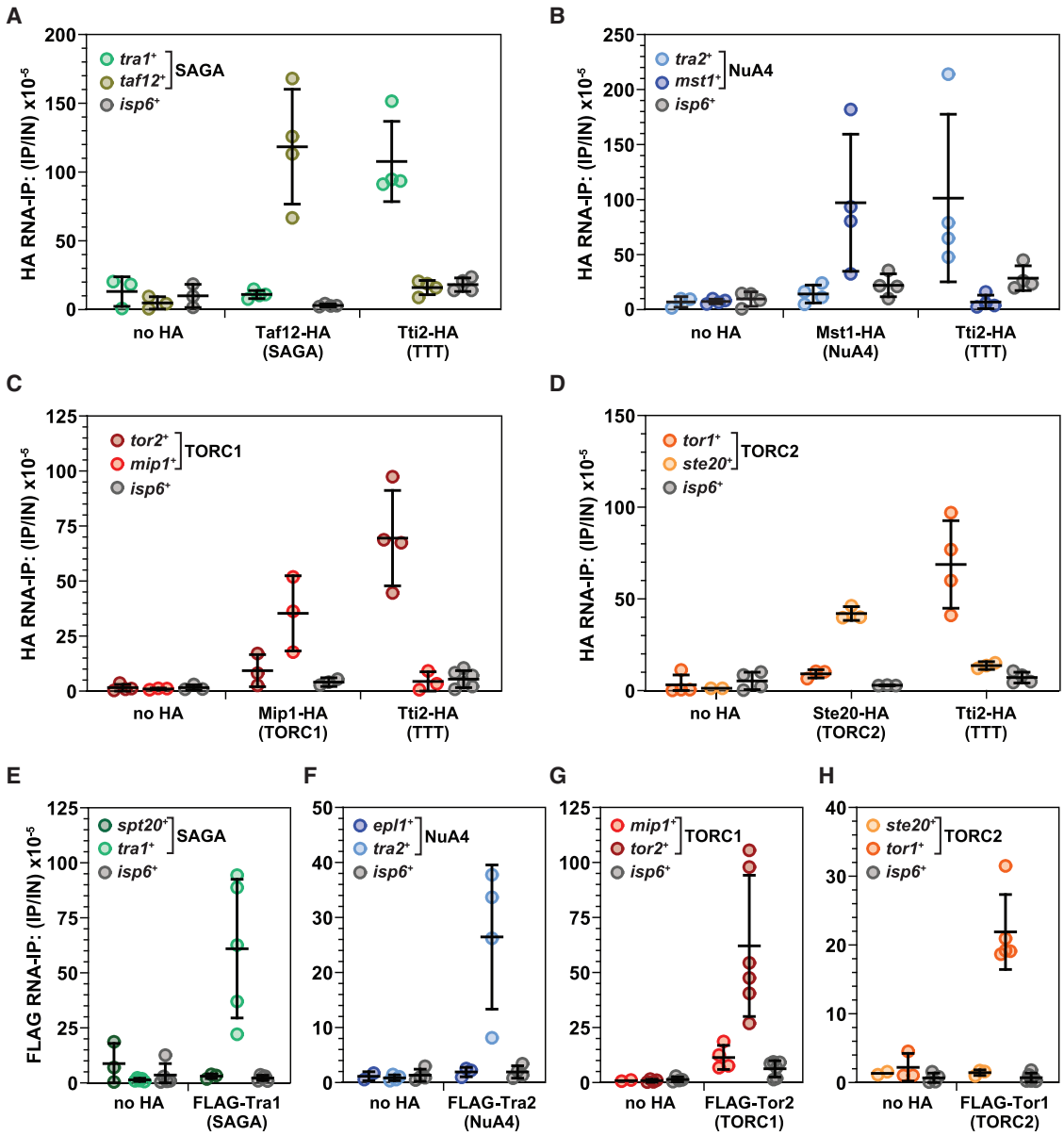

Figure 5. PIKKs do not assemble cotranslationally

SAGA, NuA4, TORC1, and TORC2 subunit RIP-qPCR analyzed as described in Figure 2. IP/IN ratios from independent experiments are shown as individual points ($n \geq 3$) overlaid with the mean and SD.

(A) *tra1*+ and *taf12*+ levels in Taf12-HA and Tti2-HA IPs.

(B) *tra2*+ and *epl1*+ levels in Mst1-HA and Tti2-HA IPs.

(C) *tor2*+ and *mip1*+ levels in Mip1-HA and Tti2-HA IPs.

(D) *tor1*+ and *ste20*+ levels in Ste20-HA and Tti2-HA IPs.

(E) *spt20*+ and *tra1*+ levels in FLAG-Tra1 IPs.

(F) *epl1*+ and *tra2*+ levels in FLAG-Tra2 IPs.

(G) *mip1*+ and *tor2*+ levels in FLAG-Tor2 IPs.

(H) *ste20*+ and *tor1*+ levels in FLAG-Tor1 IPs.

the HA sequence is located 5′ of a ~500 base-pair-long TAP sequence. We reasoned that this distance may be sufficient to capture Taf12, Mst1, Mip1, and Ste20 binding to their own mRNAs. Indeed, we found robust enrichment of *taf12*$^+$, *mst1*$^+$, *mip1*$^+$, and *ste20*$^+$ in the corresponding RIPs (Figures 5A–5D).

As a putative control for cotranslational interaction, we also tested whether each bait interacts with mRNAs encoding other subunits from each complex. For SAGA, we found no enrichment of both *ada1*$^+$ and *spt20*$^+$ in Taf12 RIPs (Figure S6A), although these subunits interact directly with each other within the

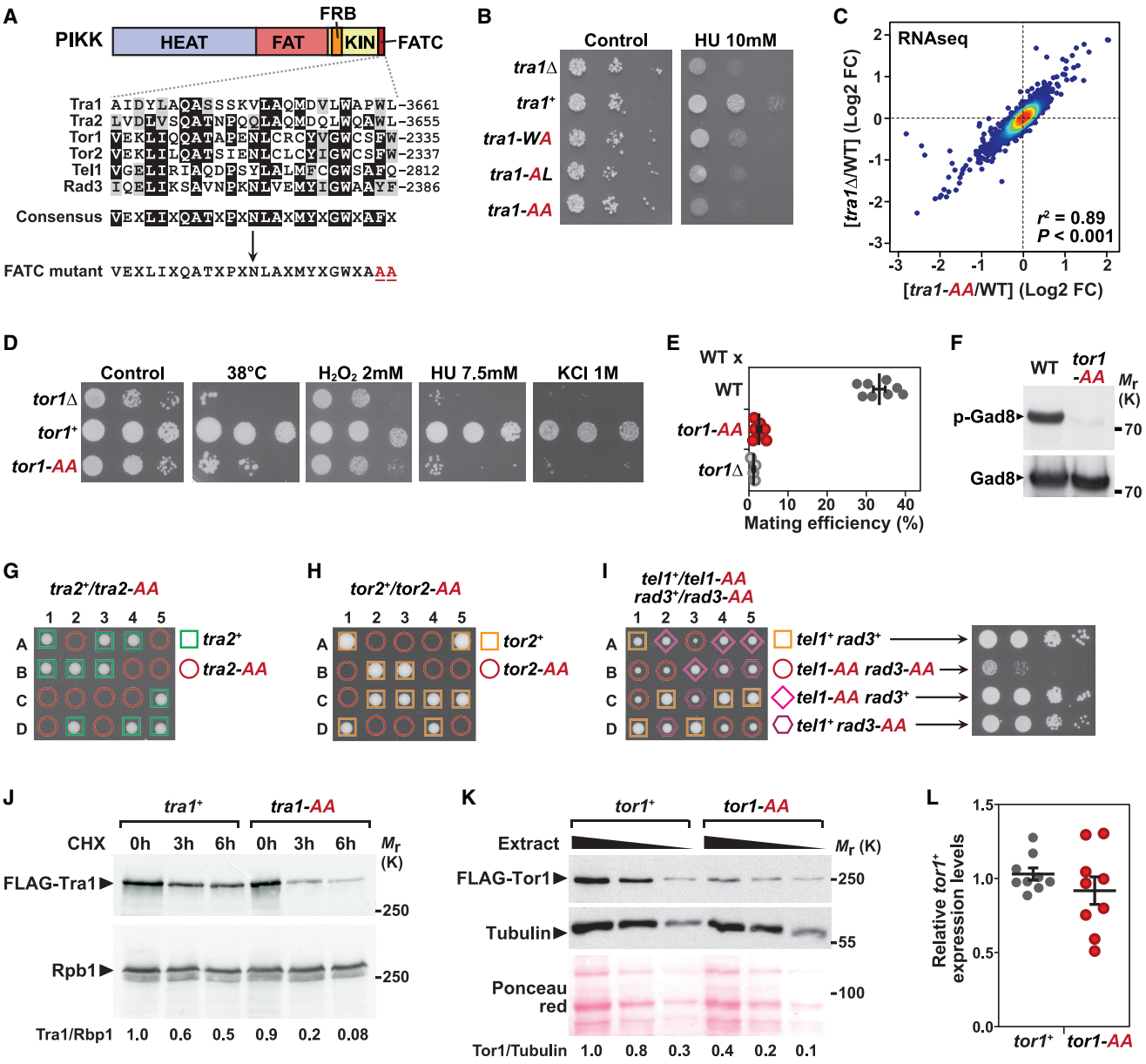

Figure 6. The C-ter FATC region is essential for PIKK function and stability

(A) Multiple alignments of the FATC region of *S. pombe* Tra1 (SPBP16F5.03c), Tra2 (SPAC1F5.11c), Tor1 (SPBC30D10.10c), Tor2 (SPBC216.07c), Tel1 (SPCC23B6.03c), and Rad3 (SPBC216.05). Residues that are identical or similar to the consensus sequence are shaded in black or gray, respectively, using Boxshade 3.2. X indicates residues that are not conserved. PIKK-FATC mutant alleles were constructed by substituting the last two hydrophobic residues with alanine.

(B) Hydroxyurea (HU) sensitivity of *tra1-WA*, *tra1-AL*, *tra1-AA*, and *tra1*Δ mutants. Ten-fold serial dilutions of exponentially growing cells were spotted on rich medium supplemented with 10 mM HU and incubated for 3 days at 32°C.

(C) Density scatterplots from RNA-seq count data comparing *tra1-AA* (x axis) with *tra1*Δ mutants (y axis), relative to isogenic WT controls (n = 3). Statistical significance and correlation were estimated with the Pearson correlation coefficient (r^2 = 0.89, p < 0.001).

(D) Growth of WT, *tor1-AA*, and *tor1*Δ strains in stress conditions. Ten-fold serial dilutions of exponentially growing cells were spotted on rich medium (control), incubated at 32°C or 38°C, or supplemented with 2 mM H_2O_2, 7.5 mM HU, or 1 mM KCl.

(E) Mating assays showing the percentage of zygotes and tetrads counted after backcrossing WT, *tor1-AA*, and *tor1*Δ strains with a WT partner. 300 cells were counted in each independent experiment, which are shown as individual points (n = 8) overlaid with the mean and SD.

(F) Gad8 phosphorylation levels (P-Gad8) in WT and *tor1-AA* strains in which endogenous Gad8 is HA-tagged. Western blots of protein extracts were probed with anti-P-Gad8 and anti-HA antibodies.

(G and H) Heterozygous *tra2+/tra2-AA* (G) *tor2+/tor2-AA* (H) diploid strains were sporulated, dissected, and germinated to show a 2:2 segregation of a lethal phenotype.

(legend continued on next page)

complex (Papai et al., 2020). For NuA4, we observed that *epl1*$^+$, but not *vid21*$^+$, is robustly enriched in Mst1 RIPs compared with a control purification (Figure S6B). This result is consistent with the observation that Epl1 directly interacts with Mst1 within the HAT module (Xu et al., 2016) and suggests that these subunits might assemble cotranslationally. Finally, for TORC1 and TORC2, we found no detectable enrichment of *toc1*$^+$ and *sin1*$^+$ in RIPs of the TORC1 subunit Mip1 and the TORC2 subunit Ste20, respectively (Figures S6C and S6D).

Cotranslational interactions typically occur unidirectionally, with only one subunit binding to the nascent polypeptide of the interacting partner (Natan et al., 2017). We therefore tested whether PIKKs engage with nascent polypeptides of SAGA, NuA4, TORC1, and TORC2 subunits, rather than partners engaging with nascent PIKKs. For this, we performed RIPs of Tra1, Tra2, Tor2, and Tor1 using strains in which each endogenous PIKK is N-ter-tagged. qRT-PCR analyses showed no interaction for the tested pairwise combinations (Figures 5E–5H) compared with a control no-tag purification and *isp6*$^+$. As a positive control, we found robust enrichment of each PIKK mRNA upon its own purification.

In conclusion, the nascent Tra1, Tra2, Tor2, and Tor1 polypeptides interact specifically with TTT, but not with their interacting partners within SAGA, NuA4, TORC1, or TORC2. Furthermore, we found no evidence supporting the cotranslational assembly of PIKKs into their complexes.

The C-ter FATC region is essential for PIKK functions

Our observations suggest a model by which TTT promotes the cotranslational maturation of PIKKs early during their biogenesis, before they incorporate into a functional complex. We next sought to understand why PIKK biogenesis follows an ordered pathway in which folding and assembly would occur sequentially. A distinctive feature of all PIKKs is the ~30-residue-long FATC region at their C-ter end (Figure 6A), where highly conserved hydrophobic residues form a helical structure buried inside the protein, close to the catalytic site (Imseng et al., 2018). We reasoned that the C-ter FATC region might be important for PIKKs to adopt their native state and interact with their partners, and, consequently, that the final steps of PIKK folding only proceed once translation has been completed.

This hypothesis predicts that the FATC region is essential for PIKK stability and functions. Previous studies in different organisms have reported that mutations in this region affect PIKK expression and activity (DaSilva et al., 2013; Genereaux et al., 2012; Hoke et al., 2010; Morita et al., 2007; Priestley et al., 1998; Takahashi et al., 2000). To strengthen these observations, we systematically tested the effect of mutating the FATC of each PIKK in *S. pombe*. Specifically, we substituted the last two residues of the FATC, and hence of the entire protein, with alanine residues in Tra1, Tra2, Tor2, Tor1, Rad3, and Tel1 (Figure 6A).

Phenotypic analyses of *tra1-AA* mutants, as well as of strains carrying single *tra1-WA* and *tra1-AL* mutations, showed that all *tra1* FATC mutants are sensitive to replicative stress, similar to *tra1*Δ deletion mutants (Figure 6B). Likewise, using RNA sequencing (RNA-seq), we found a positive correlation between the changes observed in *tra1-AA* and *tra1*Δ mutants compared with a wild-type (WT) control strain (Figure 6C). Similarly, *tor1* FATC mutants phenocopied *tor1*Δ deletion mutants in all conditions tested, including oxidative stress, replicative stress, high osmolarity, and high temperature (Figure 6D). In addition, both *tor1-AA* and *tor1*Δ mutants are defective in mating (Figure 6E). Last, phosphorylation of a canonical TORC2 substrate, the *S. pombe* AKT ortholog Gad8, is almost undetectable in extracts from *tor1-AA* mutants (Figure 6F).

Both Tra2 and Tor2 are essential for viability in *S. pombe* (Helmlinger et al., 2011; Weisman and Choder, 2001). To test the role of their FATC regions, we generated either *tra2+/tra2-AA* or *tor2+/tor2-AA* heterozygous diploids, which sporulation showed 2:2 segregation of a lethality phenotype (Figures 6G and 6H). Marker analysis confirmed that the genotype of all viable spores is WT for *tra2*$^+$ and *tor2*$^+$. An identical phenotype is observed in *tra2*$^+$/*tra2*Δ diploids (Helmlinger et al., 2011) and *tor2*$^+$/*tor2*Δ diploids (Weisman and Choder, 2001), indicating that *tra2-AA* and *tor2-AA* mutants phenocopy *tra2*$^+$ and *tor2*$^+$ deletions, respectively.

Finally, we characterized the growth phenotypes of strains simultaneously carrying FATC mutations in the *rad3*$^+$ and *tel1*$^+$ genes. Indeed, *rad3*Δ *tel1*Δ double-deletion mutants show a severe growth phenotype in standard conditions (Naito et al., 1998). For this, we crossed *rad3-AA* and *tel1-AA* strains to generate *rad3*$^+$/*rad3-AA tel1*$^+$/*tel1-AA* double heterozygous diploids. Sporulation and marker segregation analyses demonstrated that *rad3-AA tel1-AA* double mutants have severe growth defects in rich media compared with *rad3-AA* and *tel1-AA* single mutants, and WT controls (Figure 6I). Altogether, our comprehensive genetic analysis demonstrates that mutating the last two residues of all PIKKs phenocopies the loss-of-function phenotypes observed in the corresponding deletion mutants. The C-ter residues of PIKKs are therefore essential for their functions.

The C-ter FATC region is critical for PIKK stability

We then determined the effect of PIKK C-ter residues on their stability. For this, we performed western blot analyses of the endogenously FLAG-tagged Tra1-AA and Tor1-AA mutants.

(I) *tel1+/tel1-AA rad3+/rad3-AA* double heterozygous diploid strains were sporulated, dissected, and germinated to show the growth phenotype of all four possible genotypes. Each spore colony from one tetrad was isolated, and ten-fold serial dilutions of exponentially growing cells were spotted on rich medium.
(J) FLAG-Tra1 stability in WT (*tra1+*) and *tra1-AA* mutant strains grown to the exponential phase in rich medium and treated with 100 μM CHX for 3 and 6 h. Western blots of protein extracts were probed with anti-FLAG and anti-Rpb1 antibodies. Numbers below show the mean signal intensity of Tra1 normalized to Rpb1 (n = 3).
(K) FLAG-Tor1 steady-state levels in WT (*tor1+*) and *tor1-AA* mutant strains grown to the exponential phase in rich medium. Western blots of 2-fold dilutions of protein extracts were probed with anti-FLAG and anti-tubulin antibodies. Ponceau red served as a loading control. Numbers below show the mean signal intensity of Tor1 normalized to tubulin (n = 3).
(L) qRT-PCR of *tor1+* mRNA in WT (*tor1+*) and *tor1-AA* mutant strains grown to the exponential phase in rich medium. *act1+* served as internal control for normalization across samples. Values from independent experiments are shown as individual points (n = 9) overlaid with the mean and SD.

Compared with Tra1, we observed normal steady-state levels of the Tra1-AA protein, but a CHX chase showed decreased stability (Figure 6J). We found that Tor1-AA levels decrease already at steady state about 2- to 3-fold compared with Tor1 (Figure 6K). We were unable to perform a CHX chase of Tor1-AA, likely because of their slow growth. qRT-PCR analyses revealed that *tor1*$^{+}$ mRNA levels do not change in *tor1-AA* mutants (Figure 6L), indicating that mutating the FATC region affects Tor1 protein levels specifically. By analogy with Tra1-AA, we speculate that this observation is explained by decreased stability of Tor1-AA, although we cannot exclude that these mutations affect its synthesis. In conclusion, the loss-of-function phenotypes observed when the Tra1 and Tor1 hydrophobic C-ter ends are mutated likely result from protein misfolding and degradation.

Supporting this conclusion, we found that Tra1 FATC mutants cannot interact with SAGA (Figures S7A and S7B). Silver staining and quantitative TAP-MS analyses showed that Tra1 is absent from SAGA purified from *tra1-AA* and *tra1-1* strains, in which the FATC is mutated and deleted, respectively. As expected, similar results were obtained in *tra1* mutants with longer C-ter truncations that remove the KIN and FAT domains. We verified that the levels of the bait, Spt7, were comparable across strains. The effect of the FATC region on Tra1 incorporation into SAGA is indirect, because we previously identified a short, 40-residue region at the start of the FAT domain that mediates its interaction with SAGA (Elías-Villalobos et al., 2019a). Examination of the *S. cerevisiae* Tra1 structure shows that these residues are located about 45 Å from the FATC region and have no direct intramolecular contacts with the FATC (PDB: 5OJS) (Díaz-Santín et al., 2017).

TTT recognizes PIKKs in a non-native state during translation

Overall, we accumulated functional and biochemical evidence confirming the structural importance of the hydrophobic residues at the C-ter end of PIKKs. This property implies that the nascent PIKK polypeptide, at least the FATKIN unit, stays in a non-native state during translation until ribosomes reach the end of the transcript and produce the FATC region. We thus hypothesized that TTT acts as a bona fide chaperone, binding to nascent PIKKs in a non-native state.

To test this, we assessed the interaction between TTT and PIKK FATC mutants, which are likely misfolded (Figures 6, S7A, and S7B). Quantitative TAP-MS showed that Tti2 interacts with both Tra1-AA and Tor1-AA mutants, similar to WT controls (Figures 7A and 7B). RIP-qPCR analyses indicated that Tti2 binds to both *tra1-AA* and *tor1-AA* mRNAs compared with a control no-tag purification and *isp6*$^{+}$ (Figures 7C and 7D). Western blotting confirmed that Tti2 levels are comparable among all mutants in both total extracts and purification eluates (Figure S7C). Tti2 interaction with *tra1-AA* is reduced about two-fold compared with Tra1, contrasting with results from protein-protein interaction experiments. Regardless, these observations indicate that Tti2 is able to recognize and engage with misfolded forms of Tra1 and Tor1. Furthermore, in contrast to what we observed for SAGA (Figures S7A and S7B), TTT does not require an intact FATC region for interaction (Figures 3 and 7), suggesting that SAGA and TTT recognize Tra1 in distinct structural conformations. Together with our observations that TTT and SAGA subunits likely interact with Tra1 in a mutually exclusive manner, these results indicate that TTT is a cotranslational chaperone of PIKKs.

DISCUSSION

Seminal work in yeast and mammals established that the TTT complex is an Hsp90 cochaperone dedicated to the stabilization of PIKKs (Hayashi et al., 2007; Takai et al., 2007). Here we provide mechanistic insights into how TTT regulates PIKK biogenesis. Our work suggests a model by which TTT acts at a late step during PIKK translation and is important to ensure that folding is completed before assembly, rather than concurrently (Figure 7E). TTT would maintain nascent PIKKs in a non-native state during synthesis of the FAT and KIN domains, until the last residues are released by the ribosome. These residues form the highly conserved C-ter FATC region, whose hydrophobicity is essential for the final steps of PIKK folding. This model has two important implications. First, PIKK maturation is most likely completed after translation termination. Second, nascent PIKKs should not engage in cotranslational interactions with their partners, which we verified experimentally. We thus propose a general principle of PIKK biogenesis by which folding and maturation are coupled to translation, whereas incorporation into a functional complex occurs at a later step (Figure 7E). Our study contributes to better understand of how chaperones control the maturation of specific classes of substrates and the assembly of multimeric complexes.

We established that TTT binds to its substrates cotranslationally in fission yeast, indicating that TTT acts early during PIKK biogenesis. Additional evidence supports this conclusion. First, protein-protein and protein-RNA interaction analyses correlated remarkably well (Figures 3 and S4). Second, work in mammalian cells showed that TELO2 binds newly synthesized PIKKs and promotes the formation of nascent MTOR complexes (Takai et al., 2010). Likewise, in *S. pombe*, Tti2 is essential for the *de novo* assembly of Tra1 into SAGA (Elías-Villalobos et al., 2019a). This finding implies that TTT is specifically recruited to PIKK-translating polysomes, although by a mechanism that remains unclear. Our attempts to profile TTT distribution using sucrose gradient density centrifugation failed to detect an enrichment of TTT in polysomal fractions. However, this interaction is probably transient, restricted to a few polysomes, and therefore may be difficult to detect.

Together with the recent description of the human TTT structure (Pal et al., 2021), our work brings insights into how TTT interacts with PIKKs *in vivo*. First, Tti1 has a major contribution in substrate binding, consistent with its central position in the complex (Pal et al., 2021). Second, our structure-function analyses showed that TTT binds to the nascent FAT and KIN domains of Tra1, Tor1, and Tel1, although TTT may interact differently with each PIKK. The structures of PIKKs revealed an intricate network of interactions between these domains, forming a single FATKIN unit (Imseng et al., 2018), which shows the strongest sequence similarity between PIKKs (Figures 3A and S4A). It is therefore tempting to speculate that TTT recognizes all PIKKs through this unit. Conversely, this similarity may be essential for the folding of FATKIN into a topologically conserved architecture, as observed

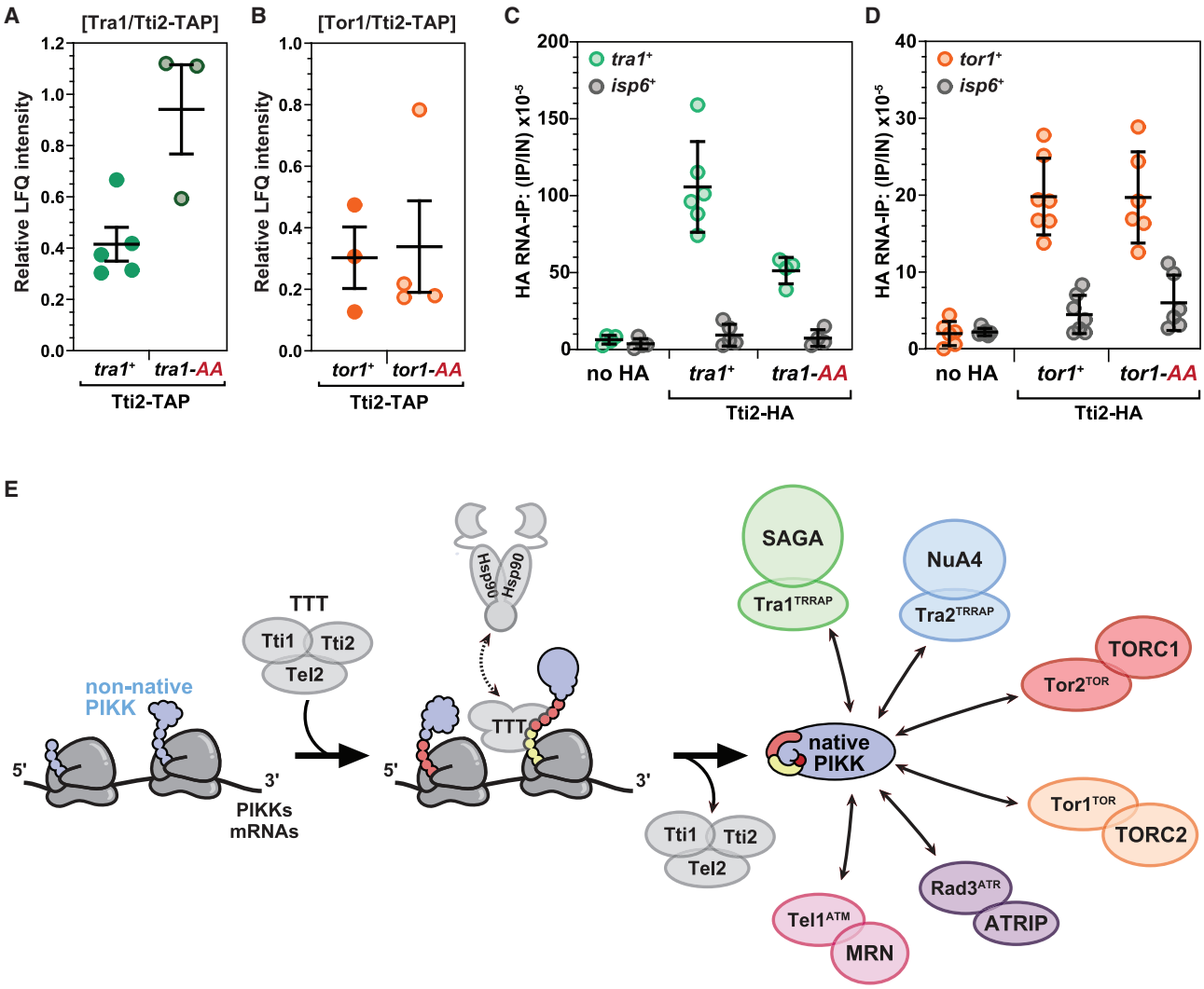

Figure 7. TTT recognizes PIKKs in a non-native state during translation

(A and B) LC-MS/MS analysis of Tti2 purified from WT, *tra1-AA* (A), and *tor1-AA* (B) strains. LFQ ratios of Tra1 or Tor1 to Tti2 from at least three independent experiments ($n \geq 3$) are plotted individually with the mean.

(C and D) RIP-qPCR of *tra1+* (C) and *tor1+* (D) mRNAs in Tti2-HA purified from WT, *tra1-AA* (C), and *tor1-AA* (D) strains, analyzed as described in Figure 2. IP/IN ratios from independent experiments are shown as individual points ($n \geq 4$) overlaid with the mean and SD.

(E) Working model for the stepwise biogenesis of PIKKs and control by the Hsp90 cochaperone TTT. See Discussion for details.

in structural studies (Imseng et al., 2018). We thus propose that TTT recognizes a specific, non-native conformation adopted by the FAT and KIN domains as they emerge from polysomes, rather than particular sequence motifs. Surprisingly, TTT does not interact with the HEAT repeats, although they represent more than half of each PIKK, form a massive super-helical structure, and make extensive contacts with other domains that are essential for the native structure. Interestingly, their sequence and structure are more variable between PIKKs (Imseng et al., 2018), suggesting that they might be chaperoned by specific factors, such as PIKK partners. However, we failed to detect cotranslational interactions with subunits of PIKK complexes (Figures 4 and 5). The HEAT repeats may thus require either general ribosome-associated chaperones or an unknown, dedicated assembly factor.

The observation that PIKKs do not engage in cotranslational interactions with their partners was somewhat surprising, because recent studies established that cotranslational assembly is a prevalent mechanism for promoting protein-protein interactions (Duncan and Mata, 2011; Shiber et al., 2018). In contrast, PIKK complexes use both dedicated factors and cotranslational engagement of subunits for their assembly. For example, we show here that NuA4 assembly involves both the TTT cochaperone for Tra2 and the cotranslational interactions between Mst1 and Epl1. Why would PIKKs require a dedicated factor for cotranslational maturation, rather than the chaperoning activity of their interacting partners? We propose that the presence of hydrophobic residues at the C-ter end of the protein dictates this choice. Although this region is an integral part of the KIN domain,

positioned adjacent to the activation loop, its disruption affects both active and inactive PIKKs similarly (Figure 6), suggesting that its primary role is structural rather than regulatory. Consequently, despite their large size, nascent PIKKs remain in a non-native state during translation and cannot engage in premature interactions with their partners. TTT might therefore prevent PIKK partners from binding prematurely to nascent PIKKs. Several regions from the FAT and KIN domains make direct contact with interacting subunits, particularly for SAGA and NuA4 (Papai et al., 2020; Sharov et al., 2017; Wang et al., 2018, 2020). In this model, the hydrophobic FATC region would be essential for PIKK incorporation by promoting the dissociation of TTT from the FATKIN after translation, thereby uncovering interaction surfaces for binding partners.

Finally, our observation that TTT and PIKK partners do not stably interact suggests that TTT might not be directly involved in PIKK complex assembly. These interactions might be transient, and we cannot exclude a role of TTT. However, other factors likely help PIKK complexes acquire their quaternary structures. An obvious candidate is the Particle for Arrangement of Quaternary structure (PAQosome), which comprises the R2TP and Prefoldin-like complexes and promotes the formation of various multimeric complexes (Houry et al., 2018; Muñoz-Hernández et al., 2018). Surprisingly, however, both RPAP3 and PIH1D1 lack orthologs in *Schizosaccharomyces* genomes, despite their widespread conservation in all major eukaryotic clades. One possibility is that Asa1 functionally compensates for the absence of R2TP in *S. pombe*. Asa1 copurifies with TTT (Figure 1) and interacts genetically and physically with TTT and PIKKs (Goto et al., 2017; Rozario and Siede, 2012; Stirling et al., 2011). To conclude, studying how TTT, its partners, and the network of associated chaperones control the cotranslational maturation and assembly of PIKKs will continue to bring insights into the biogenesis, function, and regulation of large multimeric complexes.

STAR★METHODS

Detailed methods are provided in the online version of this paper and include the following:

- KEY RESOURCES TABLE
- RESOURCE AVAILABILITY
  - Lead contact
  - Materials availability
  - Data and code availability
- EXPERIMENTAL MODEL AND SUBJECT DETAILS
  - *S. pombe* procedures and growth conditions
  - *S. pombe* strain construction
- METHOD DETAILS
  - Proliferation and cell viability assays
  - RT-qPCR analysis
  - Protein extraction
  - Western blotting and antibodies
  - Chromatin immunoprecipitation
  - RNA immunoprecipitation
  - Affinity purification
  - Mass spectrometry and data analysis
  - RNA-seq and data analysis
- QUANTIFICATION AND STATISTICAL ANALYSIS

SUPPLEMENTAL INFORMATION

Supplemental information can be found online at https://doi.org/10.1016/j.celrep.2021.109867.

ACKNOWLEDGMENTS

We thank K. Wagner for technical assistance and all members of the laboratory for helpful discussions. We are grateful to R. Allshire, H. Masukata, J. Petersen, S. Coulon, and the YGRC (NBRP, Japan) for sharing strains and reagents. We thank C. Duncan and J. Mata for assistance with RIPs. D.T. was a recipient of fellowships from Labex EpiGenMed, an Investissements d'avenir program (ANR-10-LABX-12-01), and the Ligue Contre le Cancer. A.E.-V. was a recipient of a postdoctoral fellowship from the Fondation pour la Recherche Médicale. This work was supported by funds from the Agence Nationale de la Recherche (ANR-15-CE12-0009-01 and ANR-15-CE11-0022-03) and the Fondation ARC (PJA 20181208277) to D.H.

AUTHOR CONTRIBUTIONS

A.E.-V., D.T., and A.N. designed, performed, and analyzed the experiments. C.F. and G.L. implemented TAP-MS. M.S. conducted quantitative liquid chromatography-tandem mass spectrometry (LC-MS/MS). D.H. acquired funding, supervised the project, and wrote the paper, with input from all authors.

DECLARATION OF INTERESTS

The authors declare no competing interests.

Received: November 16, 2020
Revised: July 30, 2021
Accepted: September 30, 2021
Published: October 19, 2021

REFERENCES

Ahmed, S., Alpi, A., Hengartner, M.O., and Gartner, A. (2001). *C. elegans* RAD-5/CLK-2 defines a new DNA damage checkpoint protein. Curr. Biol. *11*, 1934–1944.

Alvarez, B., and Moreno, S. (2006). Fission yeast Tor2 promotes cell growth and represses cell differentiation. J. Cell Sci. *119*, 4475–4485.

Anders, S., Pyl, P.T., and Huber, W. (2015). HTSeq—a Python framework to work with high-throughput sequencing data. Bioinformatics *31*, 166–169.

Anderson, C.M., Korkin, D., Smith, D.L., Makovets, S., Seidel, J.J., Sali, A., and Blackburn, E.H. (2008). Tel2 mediates activation and localization of ATM/Tel1 kinase to a double-strand break. Genes Dev. *22*, 854–859.

Antonova, S.V., Haffke, M., Corradini, E., Mikuciunas, M., Low, T.Y., Signor, L., van Es, R.M., Gupta, K., Scheer, E., Vos, H.R., et al. (2018). Chaperonin CCT checkpoint function in basal transcription factor TFIID assembly. Nat. Struct. Mol. Biol. *25*, 1119–1127.

Ashkenazy, H., Abadi, S., Martz, E., Chay, O., Mayrose, I., Pupko, T., and Ben-Tal, N. (2016). ConSurf 2016: an improved methodology to estimate and visualize evolutionary conservation in macromolecules. Nucleic Acids Res. *44* (*W1*), W344–W350.

Bähler, J., Wu, J.Q., Longtine, M.S., Shah, N.G., McKenzie, A., 3rd, Steever, A.B., Wach, A., Philippsen, P., and Pringle, J.R. (1998). Heterologous modules for efficient and versatile PCR-based gene targeting in *Schizosaccharomyces pombe*. Yeast *14*, 943–951.

Blackford, A.N., and Jackson, S.P. (2017). ATM, ATR, and DNA-PK: The Trinity at the Heart of the DNA Damage Response. Mol. Cell *66*, 801–817.

Brown, M.C., and Gromeier, M. (2017). MNK Controls mTORC1:Substrate Association through Regulation of TELO2 Binding with mTORC1. Cell Rep. *18*, 1444–1457.

Bustin, S.A., Benes, V., Garson, J.A., Hellemans, J., Huggett, J., Kubista, M., Mueller, R., Nolan, T., Pfaffl, M.W., Shipley, G.L., et al. (2009). The MIQE guidelines: minimum information for publication of quantitative real-time PCR experiments. Clin. Chem. *55*, 611–622.

Cox, J., and Mann, M. (2008). MaxQuant enables high peptide identification rates, individualized p.p.b.-range mass accuracies and proteome-wide protein quantification. Nat. Biotechnol. *26*, 1367–1372.

Cox, J., Neuhauser, N., Michalski, A., Scheltema, R.A., Olsen, J.V., and Mann, M. (2011). Andromeda: a peptide search engine integrated into the MaxQuant environment. J. Proteome Res. *10*, 1794–1805.

DaSilva, L.F., Pillon, S., Genereaux, J., Davey, M.J., Gloor, G.B., Karagiannis, J., and Brandl, C.J. (2013). The C-terminal residues of *Saccharomyces cerevisiae* Mec1 are required for its localization, stability, and function. G3 (Bethesda) *3*, 1661–1674.

David-Morrison, G., Xu, Z., Rui, Y.-N., Charng, W.-L., Jaiswal, M., Yamamoto, S., Xiong, B., Zhang, K., Sandoval, H., Duraine, L., et al. (2016). WAC Regulates mTOR Activity by Acting as an Adaptor for the TTT and Pontin/Reptin Complexes. Dev. Cell *36*, 139–151.

Detilleux, D., Raynaud, P., Pradet-Balade, B., and Helmlinger, D. (2021). The TRRAP transcription cofactor represses interferon-stimulated genes in colorectal cancer cells. BioRxiv.

Díaz-Santín, L.M., Lukoyanova, N., Aciyan, E., and Cheung, A.C. (2017). Cryo-EM structure of the SAGA and NuA4 coactivator subunit Tra1 at 3.7 angstrom resolution. eLife *6*, 1–20.

Duncan, C.D., and Mata, J. (2011). Widespread cotranslational formation of protein complexes. PLoS Genet. *7*, e1002398.

Duncan, C.D., and Mata, J. (2014). Cotranslational protein-RNA associations predict protein-protein interactions. BMC Genomics *15*, 298.

Elías-Villalobos, A., Toullec, D., Faux, C., Séveno, M., and Helmlinger, D. (2019a). Chaperone-mediated ordered assembly of the SAGA and NuA4 transcription co-activator complexes in yeast. Nat. Commun. *10*, 5237.

Elías-Villalobos, A., Fort, P., and Helmlinger, D. (2019b). New insights into the evolutionary conservation of the sole PIKK pseudokinase Tra1/TRRAP. Biochem. Soc. Trans. *47*, 1597–1608.

Fernández-Sáiz, V., Targosz, B.-S.S., Lemeer, S., Eichner, R., Langer, C., Bullinger, L., Reiter, C., Slotta-Huspenina, J., Schroeder, S., Knorn, A.-M.M., et al. (2013). SCFFbxo9 and CK2 direct the cellular response to growth factor withdrawal via Tel2/Tti1 degradation and promote survival in multiple myeloma. Nat. Cell Biol. *15*, 72–81.

Forsburg, S.L., and Rhind, N. (2006). Basic methods for fission yeast. Yeast *23*, 173–183.

Funakoshi, M., Tomko, R.J., Jr., Kobayashi, H., and Hochstrasser, M. (2009). Multiple assembly chaperones govern biogenesis of the proteasome regulatory particle base. Cell *137*, 887–899.

Genereaux, J., Kvas, S., Dobransky, D., Karagiannis, J., Gloor, G.B., and Brandl, C.J. (2012). Genetic evidence links the ASTRA protein chaperone component Tti2 to the SAGA transcription factor Tra1. Genetics *191*, 765–780.

Goto, G.H., Ogi, H., Biswas, H., Ghosh, A., Tanaka, S., and Sugimoto, K. (2017). Two separate pathways regulate protein stability of ATM/ATR-related protein kinases Mec1 and Tel1 in budding yeast. PLoS Genet. *13*, e1006873.

Gueldener, U., Heinisch, J., Koehler, G.J., Voss, D., and Hegemann, J.H. (2002). A second set of loxP marker cassettes for Cre-mediated multiple gene knockouts in budding yeast. Nucleic Acids Res. *30*, e23.

Halbach, A., Zhang, H., Wengi, A., Jablonska, Z., Gruber, I.M.L.L., Halbeisen, R.E., Dehé, P.-M.M., Kemmeren, P., Holstege, F., Géli, V., et al. (2009). Co-translational assembly of the yeast SET1C histone methyltransferase complex. EMBO J. *28*, 2959–2970.

Hayashi, T., Hatanaka, M., Nagao, K., Nakaseko, Y., Kanoh, J., Kokubu, A., Ebe, M., and Yanagida, M. (2007). Rapamycin sensitivity of the *Schizosaccharomyces pombe* tor2 mutant and organization of two highly phosphorylated TOR complexes by specific and common subunits. Genes Cells *12*, 1357–1370.

Helmlinger, D., Marguerat, S., Villén, J., Gygi, S.P., Bähler, J., and Winston, F. (2008). The *S. pombe* SAGA complex controls the switch from proliferation to sexual differentiation through the opposing roles of its subunits Gcn5 and Spt8. Genes Dev. *22*, 3184–3195.

Helmlinger, D., Marguerat, S., Villén, J., Swaney, D.L., Gygi, S.P., Bähler, J., and Winston, F. (2011). Tra1 has specific regulatory roles, rather than global functions, within the SAGA co-activator complex. EMBO J. *30*, 2843–2852.

Hentges, P., Van Driessche, B., Tafforeau, L., Vandenhaute, J., and Carr, A.M. (2005). Three novel antibiotic marker cassettes for gene disruption and marker switching in *Schizosaccharomyces pombe*. Yeast *22*, 1013–1019.

Hoffman, K.S., Duennwald, M.L., Karagiannis, J., Genereaux, J., McCarton, A.S., and Brandl, C.J. (2016). *Saccharomyces cerevisiae* Tti2 Regulates PIKK Proteins and Stress Response. G3 (Bethesda) *6*, 1649–1659.

Hoke, S.M., Irina Mutiu, A., Genereaux, J., Kvas, S., Buck, M., Yu, M., Gloor, G.B., and Brandl, C.J. (2010). Mutational analysis of the C-terminal FATC domain of *Saccharomyces cerevisiae* Tra1. Curr. Genet. *56*, 447–465.

Hořejší, Z., Takai, H., Adelman, C.A., Collis, S.J., Flynn, H., Maslen, S., Skehel, J.M., de Lange, T., and Boulton, S.J. (2010). CK2 phospho-dependent binding of R2TP complex to TEL2 is essential for mTOR and SMG1 stability. Mol. Cell *39*, 839–850.

Houry, W.A., Bertrand, E., and Coulombe, B. (2018). The PAQosome, an R2TP-Based Chaperone for Quaternary Structure Formation. Trends Biochem. Sci. *43*, 4–9.

Hurov, K.E., Cotta-Ramusino, C., and Elledge, S.J. (2010). A genetic screen identifies the Triple T complex required for DNA damage signaling and ATM and ATR stability. Genes Dev. *24*, 1939–1950.

Imseng, S., Aylett, C.H., and Maier, T. (2018). Architecture and activation of phosphatidylinositol 3-kinase related kinases. Curr. Opin. Struct. Biol. *49*, 177–189.

Inoue, H., Sugimoto, S., Takeshita, Y., Takeuchi, M., Hatanaka, M., Nagao, K., Hayashi, T., Kokubu, A., Yanagida, M., and Kanoh, J. (2017). CK2 phospho-independent assembly of the Tel2-associated stress-signaling complexes in *Schizosaccharomyces pombe*. Genes Cells *22*, 59–70.

Izumi, N., Yamashita, A., Hirano, H., and Ohno, S. (2012). Heat shock protein 90 regulates phosphatidylinositol 3-kinase-related protein kinase family proteins together with the RUVBL1/2 and Tel2-containing co-factor complex. Cancer Sci. *103*, 50–57.

Kaizuka, T., Hara, T., Oshiro, N., Kikkawa, U., Yonezawa, K., Takehana, K., Iemura, S., Natsume, T., and Mizushima, N. (2010). Tti1 and Tel2 are critical factors in mammalian target of rapamycin complex assembly. J. Biol. Chem. *285*, 20109–20116.

Kamenova, I., Mukherjee, P., Conic, S., Mueller, F., El-Saafin, F., Bardot, P., Garnier, J.-M., Dembele, D., Capponi, S., Timmers, H.T.M., et al. (2019). Co-translational assembly of mammalian nuclear multisubunit complexes. Nat. Commun. *10*, 1740.

Kanke, M., Nishimura, K., Kanemaki, M., Kakimoto, T., Takahashi, T.S., Nakagawa, T., and Masukata, H. (2011). Auxin-inducible protein depletion system in fission yeast. BMC Cell Biol. *12*, 8.

Kassem, S., Villanyi, Z., and Collart, M.A. (2017). Not5-dependent co-translational assembly of Ada2 and Spt20 is essential for functional integrity of SAGA. Nucleic Acids Res. *45*, 1186–1199.

Kim, S.G., Hoffman, G.R., Poulogiannis, G., Buel, G.R., Jang, Y.J., Lee, K.W., Kim, B.-Y., Erikson, R.L., Cantley, L.C., Choo, A.Y., and Blenis, J. (2013). Metabolic stress controls mTORC1 lysosomal localization and dimerization by regulating the TTT-RUVBL1/2 complex. Mol. Cell *49*, 172–185.

Kim, D., Langmead, B., and Salzberg, S.L. (2015). HISAT: a fast spliced aligner with low memory requirements. Nat. Methods *12*, 357–360. https://doi.org/10.1038/nmeth.3317.

Kramer, G., Shiber, A., and Bukau, B. (2019). Mechanisms of cotranslational maturation of newly synthesized proteins. Annu. Rev. Biochem. *88*, 337–364.

Laboucarié, T., Detilleux, D., Rodriguez-Mias, R.A., Faux, C., Romeo, Y., Franz-Wachtel, M., Krug, K., Maček, B., Villén, J., Petersen, J., and Helmlinger, D. (2017). TORC1 and TORC2 converge to regulate the SAGA co-activator in response to nutrient availability. EMBO Rep. *18*, 2197–2218.

Laribee, R.N. (2018). Transcriptional and Epigenetic Regulation by the Mechanistic Target of Rapamycin Complex 1 Pathway. J. Mol. Biol. *430*, 4874–4890.

Lempiäinen, H., and Halazonetis, T.D. (2009). Emerging common themes in regulation of PIKKs and PI3Ks. EMBO J. *28*, 3067–3073.

Lock, A., Rutherford, K., Harris, M.A., Hayles, J., Oliver, S.G., Bähler, J., and Wood, V. (2019). PomBase 2018: user-driven reimplementation of the fission yeast database provides rapid and intuitive access to diverse, interconnected information. Nucleic Acids Res. *47* (*D1*), D821–D827.

Love, M.I., Huber, W., and Anders, S. (2014). Moderated estimation of fold change and dispersion for RNA-seq data with DESeq2. Genome Biol. *15*, 550.

Madeira, F., Park, Y.M., Lee, J., Buso, N., Gur, T., Madhusoodanan, N., Basutkar, P., Tivey, A.R.N., Potter, S.C., Finn, R.D., and Lopez, R. (2019). The EMBL-EBI search and sequence analysis tools APIs in 2019. Nucleic Acids Res. *47* (*W1*), W636–W641.

Marsh, J.A., and Teichmann, S.A. (2015). Structure, dynamics, assembly, and evolution of protein complexes. Annu. Rev. Biochem. *84*, 551–575.

Marsh, J.A., Hernández, H., Hall, Z., Ahnert, S.E., Perica, T., Robinson, C.V., and Teichmann, S.A. (2013). Protein complexes are under evolutionary selection to assemble via ordered pathways. Cell *153*, 461–470.

McMahon, S.B., Van Buskirk, H.A., Dugan, K.A., Copeland, T.D., and Cole, M.D. (1998). The novel ATM-related protein TRRAP is an essential cofactor for the c-Myc and E2F oncoproteins. Cell *94*, 363–374.

Morita, T., Yamashita, A., Kashima, I., Ogata, K., Ishiura, S., and Ohno, S. (2007). Distant N- and C-terminal domains are required for intrinsic kinase activity of SMG-1, a critical component of nonsense-mediated mRNA decay. J. Biol. Chem. *282*, 7799–7808.

Muñoz-Hernández, H., Pal, M., Rodríguez, C.F., Prodromou, C., Pearl, L.H., and Llorca, O. (2018). Advances on the Structure of the R2TP/Prefoldin-like Complex. Adv. Exp. Med. Biol. *1106*, 73–83.

Naito, T., Matsuura, A., and Ishikawa, F. (1998). Circular chromosome formation in a fission yeast mutant defective in two ATM homologues. Nat. Genet. *20*, 203–206.

Natan, E., Wells, J.N., Teichmann, S.A., and Marsh, J.A. (2017). Regulation, evolution and consequences of cotranslational protein complex assembly. Curr. Opin. Struct. Biol. *42*, 90–97.

Nishimura, K., Fukagawa, T., Takisawa, H., Kakimoto, T., and Kanemaki, M. (2009). An auxin-based degron system for the rapid depletion of proteins in nonplant cells. Nat. Methods *6*, 917–922.

Pal, M., Muñoz-Hernandez, H., Bjorklund, D., Zhou, L., Degliesposti, G., Skehel, J.M., Hesketh, E.L., Thompson, R.F., Pearl, L.H., Llorca, O., and Prodromou, C. (2021). Structure of the TELO2-TTI1-TTI2 complex and its function in TOR recruitment to the R2TP chaperone. Cell Rep. *36*, 109317.

Panasenko, O.O., Somasekharan, S.P., Villanyi, Z., Zagatti, M., Bezrukov, F., Rashpa, R., Cornut, J., Iqbal, J., Longis, M., Carl, S.H., et al. (2019). Co-translational assembly of proteasome subunits in NOT1-containing assemblysomes. Nat. Struct. Mol. Biol. *26*, 110–120.

Papai, G., Frechard, A., Kolesnikova, O., Crucifix, C., Schultz, P., and Ben-Shem, A. (2020). Structure of SAGA and mechanism of TBP deposition on gene promoters. Nature *577*, 711–716.

Perez-Riverol, Y., Csordas, A., Bai, J., Bernal-Llinares, M., Hewapathirana, S., Kundu, D.J., Inuganti, A., Griss, J., Mayer, G., Eisenacher, M., et al. (2019). The PRIDE database and related tools and resources in 2019: improving support for quantification data. Nucleic Acids Res. *47* (*D1*), D442–D450.

Priestley, A., Beamish, H.J., Gell, D., Amatucci, A.G., Muhlmann-Diaz, M.C., Singleton, B.K., Smith, G.C.M., Blunt, T., Schalkwyk, L.C., Bedford, J.S., et al. (1998). Molecular and biochemical characterisation of DNA-dependent protein kinase-defective rodent mutant irs-20. Nucleic Acids Res. *26*, 1965–1973.

Rao, F., Cha, J., Xu, J., Xu, R., Vandiver, M.S., Tyagi, R., Tokhunts, R., Koldobskiy, M.A., Fu, C., Barrow, R., et al. (2014). Inositol pyrophosphates mediate the DNA-PK/ATM-p53 cell death pathway by regulating CK2 phosphorylation of Tti1/Tel2. Mol. Cell *54*, 119–132.

Rigaut, G., Shevchenko, A., Rutz, B., Wilm, M., Mann, M., and Séraphin, B. (1999). A generic protein purification method for protein complex characterization and proteome exploration. Nat. Biotechnol. *17*, 1030–1032.

Roelofs, J., Park, S., Haas, W., Tian, G., McAllister, F.E., Huo, Y., Lee, B.H., Zhang, F., Shi, Y., Gygi, S.P., and Finley, D. (2009). Chaperone-mediated pathway of proteasome regulatory particle assembly. Nature *459*, 861–865.

Rozario, D., and Siede, W. (2012). *Saccharomyces cerevisiae* Tel2 plays roles in TORC signaling and telomere maintenance that can be mutationally separated. Biochem. Biophys. Res. Commun. *417*, 1182–1187.

Saeki, Y., Toh-E, A., Kudo, T., Kawamura, H., and Tanaka, K. (2009). Multiple proteasome-interacting proteins assist the assembly of the yeast 19S regulatory particle. Cell *137*, 900–913.

Saleh, A., Schieltz, D., Ting, N., McMahon, S.B., Litchfield, D.W., Yates, J.R., 3rd, Lees-Miller, S.P., Cole, M.D., and Brandl, C.J. (1998). Tra1p is a component of the yeast Ada.Spt transcriptional regulatory complexes. J. Biol. Chem. *273*, 26559–26565.

Schindelin, J., Arganda-Carreras, I., Frise, E., Kaynig, V., Longair, M., Pietzsch, T., Preibisch, S., Rueden, C., Saalfeld, S., Schmid, B., et al. (2012). Fiji: an open-source platform for biological-image analysis. Nat. Methods *9*, 676–682.

Sharov, G., Voltz, K., Durand, A., Kolesnikova, O., Papai, G., Myasnikov, A.G., Dejaegere, A., Ben Shem, A., and Schultz, P. (2017). Structure of the transcription activator target Tra1 within the chromatin modifying complex SAGA. Nat. Commun. *8*, 1556.

Shevchenko, A., Roguev, A., Schaft, D., Buchanan, L., Habermann, B., Sakalar, C., Thomas, H., Krogan, N.J., Shevchenko, A., and Stewart, A.F. (2008). Chromatin Central: towards the comparative proteome by accurate mapping of the yeast proteomic environment. Genome Biol. *9*, R167.

Shiber, A., Döring, K., Friedrich, U., Klann, K., Merker, D., Zedan, M., Tippmann, F., Kramer, G., and Bukau, B. (2018). Cotranslational assembly of protein complexes in eukaryotes revealed by ribosome profiling. Nature *561*, 268–272.

Shieh, Y.W., Minguez, P., Bork, P., Auburger, J.J., Guilbride, D.L., Kramer, G., and Bukau, B. (2015). Operon structure and cotranslational subunit association direct protein assembly in bacteria. Science *350*, 678–680.

Shikata, M., Ishikawa, F., and Kanoh, J. (2007). Tel2 is required for activation of the Mrc1-mediated replication checkpoint. J. Biol. Chem. *282*, 5346–5355.

Smits, A.H., Jansen, P.W.T.C., Poser, I., Hyman, A.A., and Vermeulen, M. (2013). Stoichiometry of chromatin-associated protein complexes revealed by label-free quantitative mass spectrometry-based proteomics. Nucleic Acids Res. *41*, e28.

Stirling, P.C., Bloom, M.S., Solanki-Patil, T., Smith, S., Sipahimalani, P., Li, Z., Kofoed, M., Ben-Aroya, S., Myung, K., and Hieter, P. (2011). The complete spectrum of yeast chromosome instability genes identifies candidate CIN cancer genes and functional roles for ASTRA complex components. PLoS Genet. *7*, e1002057.

Takahashi, T., Hara, K., Inoue, H., Kawa, Y., Tokunaga, C., Hidayat, S., Yoshino, K., Kuroda, Y., and Yonezawa, K. (2000). Carboxyl-terminal region conserved among phosphoinositide-kinase-related kinases is indispensable for mTOR function *in vivo* and *in vitro*. Genes Cells *5*, 765–775.

Takai, H., Wang, R.C., Takai, K.K., Yang, H., and de Lange, T. (2007). Tel2 regulates the stability of PI3K-related protein kinases. Cell *131*, 1248–1259.

Takai, H., Xie, Y., de Lange, T., and Pavletich, N.P. (2010). Tel2 structure and function in the Hsp90-dependent maturation of mTOR and ATR complexes. Genes Dev. *24*, 2019–2030.

Vassilev, A., Yamauchi, J., Kotani, T., Prives, C., Avantaggiati, M.L., Qin, J., and Nakatani, Y. (1998). The 400 kDa subunit of the PCAF histone acetylase complex belongs to the ATM superfamily. Mol. Cell *2*, 869–875.

Wang, X., Ahmad, S., Zhang, Z., Côté, J., and Cai, G. (2018). Architecture of the *Saccharomyces cerevisiae* NuA4/TIP60 complex. Nat. Commun. *9*, 1147.

Wang, H., Dienemann, C., Stützer, A., Urlaub, H., Cheung, A.C.M., and Cramer, P. (2020). Structure of the transcription coactivator SAGA. Nature *577*, 717–720.

Weisman, R., and Choder, M. (2001). The fission yeast TOR homolog, tor1+, is required for the response to starvation and other stresses via a conserved serine. J. Biol. Chem. *276*, 7027–7032.

Xu, P., Li, C., Chen, Z., Jiang, S., Fan, S., Wang, J., Dai, J., Zhu, P., and Chen, Z. (2016). The NuA4 Core Complex Acetylates Nucleosomal Histone H4 through a Double Recognition Mechanism. Mol. Cell *63*, 965–975.

Xu, Y.J., Khan, S., Didier, A.C., Wozniak, M., Liu, Y., Singh, A., and Nakamura, T.M. (2019). A *tel2* Mutation That Destabilizes the Tel2-Tti1-Tti2 Complex Eliminates Rad3^{ATR} Kinase Signaling in the DNA Replication Checkpoint and Leads to Telomere Shortening in Fission Yeast. Mol. Cell. Biol. *39*, 1–19.

Zhang, X.-R., He, J.-B., Wang, Y.-Z., and Du, L.-L. (2018). A Cloning-Free Method for CRISPR/Cas9-Mediated Genome Editing in Fission Yeast. G3 (Bethesda) *8*, 2067–2077.

STAR★METHODS

KEY RESOURCES TABLE

REAGENT or RESOURCE	SOURCE	IDENTIFIER
Antibodies		
Peroxidase Anti-Peroxidase (PAP) Soluble Complex antibody produced in rabbit	Sigma	Cat#P1291; RRID:AB_1079562
anti-Calmodulin binding protein antibody (Rabbit)	ICL	Cat#RCBP-45A-Z; RRID:AB_11212268
Monoclonal Anti-α-Tubulin antibody produced in mouse ascites fluid, clone B-5-1-2	Sigma	Cat#T5168; RRID:AB_477579
Mouse monoclonal anti-FLAG antibody, clone M2	Sigma	Cat#F1804; RRID:AB_262044
Mouse monoclonal anti-Myc antibody, clone 9E11	Abcam	Cat#ab56; RRID:AB_304976
Rabbit polyclonal anti-Myc antibody	Abcam	Cat#ab9106; RRID:AB_307014
Mouse monoclonal anti-HA antibody, clone 16B12	Biolegend	Cat#901514; RRID:AB_2565336
Rabbit polyclonal anti-HA antibody	Abcam	Cat#ab9110; RRID:AB_307019
Bacterial and virus strains		
E.coli DH5α	Invitrogen	Cat#18265017
Chemicals, peptides, and recombinant proteins		
Phenylmethanesulfonyl fluoride	Sigma	Cat#P7626
bestatin	Sigma	Cat#B8385
pepstatin A	Sigma	Cat#P5318
Protein G Sepharose 4 Fast Flow	Merck	Cat#GE17-0618-01
Dynabeads Pan-Mouse IgG	ThermoFisher Scientific	Cat#11041
Methylene Blue solution	Sigma	Cat#319112
Trypsin Gold, Mass Spectrometry Grade	Promega	Cat#V5280
TRIzol Reagent	ThermoFisher Scientific	Cat#15596018
cOmplete EDTA-free cocktails tablets	Roche	Cat#04693132001
Critical commercial assays		
SuperScript III First-Strand System	ThermoFisher Scientific	Cat#18080051
Gibson Assembly Master Mix	New England Biolabs	Cat#E2611L
Purelink RNA Mini kit	ThermoFisher Scientific	Cat#12183018A
Purelink RNA Micro Scale kit	ThermoFisher Scientific	Cat#12183016
SilverQuest Silver Staining Kit	ThermoFisher Scientific	Cat#LC6070
RNeasy Mini Kit	QIAGEN	Cat#74104
TURBO DNA-free kit	Invitrogen	Cat#AM1907
Deposited data		
Illumina RNA-seq data	GEO	https://www.ncbi.nlm.nih.gov/geo/query/acc.cgi?acc=GSE183610; GSE183610
Mass spectrometry proteomics data	PRIDE	https://www.ebi.ac.uk/pride/archive/projects/PXD028351; PXD028351
Mass spectrometry proteomics data	PRIDE	https://www.ebi.ac.uk/pride/archive/projects/PXD013256; PXD013256
Experimental models: Cell lines		
S. pombe strain, DHP1242, *h+ tel2-MYC12::kanMX6*	Yeast Genetic Resource Center, National BioResource Project	FY21033

(*Continued on next page*)

Continued		
REAGENT or RESOURCE	SOURCE	IDENTIFIER
Experimental models: Organisms/strains		
S. pombe strains, see Table S4	This paper	N/A
Oligonucleotides		
Oligonucleotides, see Table S5	This paper	N/A
Recombinant DNA		
pUG6 plasmid	Euroscarf	P30114
pUG75 plasmid	Euroscarf	P30671
Software and algorithms		
RStudio	https://www.rstudio.com/	version 1.3.1056
R	https://www.r-project.org/	version 3.6.0
GraphPad Prism	https://www.graphpad.com/	version 9.2.0
MaxQuant	https://www.maxquant.org/	version 1.5.5.1

RESOURCE AVAILABILITY

Lead contact

Further information and requests for resources and reagents should be directed to and will be fulfilled by the lead contact, Dominique Helmlinger (dhelmlinger@crbm.cnrs.fr).

Materials availability

All yeast strains generated in this study are available from the lead contact upon request.

Data and code availability

- RNA-seq data have been deposited at GEO and are publicly available as of the date of publication. Accession numbers are listed in the Key resources table. Mass spectrometry proteomics data have been deposited to the ProteomeXchange Consortium via the PRIDE partner repository (Perez-Riverol et al., 2019) and are publicly available as of the date of publication. Table S6 cross-references all MaxQuant results from each figure and table with the raw data files. Accession numbers are listed in the Key resources table. All data reported in this paper will be shared by the lead contact upon request.
- This paper does not report original code.
- Any additional information required to reanalyze the data reported in this paper is available from the lead contact upon request.

EXPERIMENTAL MODEL AND SUBJECT DETAILS

S. pombe procedures and growth conditions

Standard culture media and genetic manipulations were used, as described in Forsburg and Rhind (2006). For auxin-inducible targeted protein degradation (AID), cells were grown at 25°C and treated with either 0.5 mM indol-3- acetic acid (IAA, I2886, Sigma) or ethanol. For CreER-loxP-mediated recombination, cells were treated with either 1 μM β-estradiol (E2758, Sigma) or DMSO alone for 16 hours, unless otherwise indicated. For translation inhibition, cells were treated with 1 mg/mL puromycin dihydrochloride (Santa Cruz Biotechnology, sc-108071B) and incubated for 15 minutes. For cycloheximide chase, cells were treated with 100 μM cycloheximide (C7698, Sigma).

S. pombe strain construction

All *S. pombe* strains used are listed in Table S4 and were constructed by standard procedures, using either chemical transformation or genetic crosses. Genetic crosses were performed by mating strains at 25°C on SPAS medium. Strains with gene deletions, truncations, or C-terly epitope-tagged proteins were constructed by PCR-based gene targeting of the respective open reading frame (ORF) with *kanMX6*, *natMX6 or hphMX6* cassettes, amplified from pFA6a backbone plasmids (Bähler et al., 1998; Hentges et al., 2005). For insertion of loxP sites, the same resistance cassettes were amplified from the pUG6 or pUG75 plasmids (Euroscarf #P30114, and #P30671, respectively) (Gueldener et al., 2002). Alternatively, CRISPR-Cas9-mediated genome editing was used, as described in Zhang et al. (2018), particularly for marker-less N-ter epitope tagging of *tra1+*, *tra2+*, *tor2+*, *tor1+*, *rad3+*, and *tel1+*. DNA fragments used for homologous recombination were generated by PCR, gene synthesis, and Gibson assembly cloning.

Cloning strategies and primers were designed using the online fission yeast database, PomBase (Lock et al., 2019). All primer sequences are listed in Table S5. Transformants were screened for correct integration by PCR and, when appropriate, verified by Sanger sequencing or western blotting. For each transformation, 2-4 individual clones were purified and analyzed.

Because the *tel2+*, *tti1+*, and *tti2+* genes are essential for viability in *S. pombe* (Inoue et al., 2017; Shikata et al., 2007), C-ter epitope tagging was performed in diploids, to generate heterozygous alleles. Their sporulation demonstrated that all C-terly tagged Tel2, Tti2, or Tti2 strains grew similarly to wild-type controls in all conditions tested (data not shown). The same strategy was used to construct *tra1-AA*, *tra2-AA*, *tor2-AA*, *tor1-AA*, *rad3-AA*, and *tel1-AA* mutants (Figure 6).

METHOD DETAILS

Proliferation and cell viability assays

Proliferation assays were performed by inoculating single colonies in either rich (YES) or minimal (EMM) media, growing cells at 32°C, and counting their number at different time points during the exponential phase. Cell viability was assessed using 10 μL of the colorimetric dye methylene blue, which was incubated with a 50 μL suspension of exponentially growing yeast cells resuspended in PBS 1X. The number of blue dead cells was counted under a light microscope.

RT-qPCR analysis

Reverse transcription and quantitative PCR analyses of cDNA were performed using RNA extracted from 50 mL of exponentially growing cells, as described in Laboucarié et al. (2017), and according to the MIQE guidelines (Bustin et al., 2009). Briefly, total RNA was purified using hot, acidic phenol and contaminating DNA was removed by DNase I digestion, using the TURBO DNA-free kit. 1 μg of RNA was then reverse transcribed (RT) at 55°C with random hexanucleotide primers, using the SuperScript III First-Strand System. Fluorescence-based quantitative PCR was performed with SYBR Green and used to calculate relative cDNA quantities, from the slope produced by standard curves for each primer pair, in each experiment. DNase-treated RNA samples were used as controls for the presence of genomic DNA contaminants. Standard curve slopes were comprised between −3.5 (90% efficiency) and −3.15 (110% efficiency), with an $r^2 > 0.9$. All primer sequences are listed in Table S5.

Protein extraction

Protein extracts were prepared as described in Laboucarié et al. (2017). Briefly, 10 to 25 mL cultures of exponentially growing cells were homogenized by glass bead-beating in a FastPrep (MP Biomedicals). Proteins extracted using either standard lysis buffer (WEB: 40 mM HEPES-NaOH pH 7.4, 350 mM NaCl, 0.1% NP40, and 10% glycerol) or trichloroacetic acid (TCA) precipitation. WEB was supplemented with protease inhibitors, including cOmplete EDTA-free cocktails tablets, 1 mM PMSF, 1 μg/ml bestatin, and 1 μg/ml pepstatin A.

Western blotting and antibodies

Western blotting was performed using the peroxidase-anti-peroxidase (PAP), anti-Calmodulin binding protein (CBP), anti-α-Tubulin, anti-FLAG, anti-MYC, and anti-HA antibodies. Protein concentrations were measured by the Bradford method and used to load equal amounts of proteins across samples. Ponceau red or Coomassie blue staining were used to normalize for total protein levels across samples. Quantification of signal intensity was performed using staining, film exposure, or digital acquisition that were within the linear range of detection, as verified by loading serial dilutions of one sample, and analyzed with ImageJ (Schindelin et al., 2012).

Chromatin immunoprecipitation

ChIP experiments were performed as previously described (Helmlinger et al., 2011). Briefly, cell cultures were crosslinked in 1% formaldehyde for 30 min. Cells were then broken using a FastPrep (MP Biomedicals), and the chromatin fraction was sheared to 200–500 bp fragments using a Branson sonicator for 9 cycles (10 s ON, 50 s OFF) at an amplitude of 20%. For immunoprecipitation (IP), 3-5 μg of anti-HA (16B12) or anti-Myc antibodies (9E11) were incubated overnight at 4°C with the chromatin extracts and then coupled with 50 μL of protein-G-Sepharose beads during 4h at 4°C. ChIP DNA was quantified by fluorescence-based quantitative PCR using SYBR Green, as described for RT-qPCR analysis. Input (IN) samples were diluted 200-fold while IP samples were diluted 3-fold. Relative occupancy levels were determined by dividing the IP by the IN value (IP/IN) for each amplicon. To determine the specificity of enrichment of the tagged protein, the corresponding untagged control samples were included in each ChIP experiment. All primer sequences are listed in Table S5.

RNA immunoprecipitation

RIP experiments were done as described previously in Duncan and Mata (2011), with minor modifications. Briefly, 100 mL of exponentially growing cells were harvested and broken using a FastPrep (MP Biomedicals). Immunoprecipitation (IP) was performed using Dynabeads® Pan-Mouse IgG that were pre-incubated with 3 μg of anti-HA (16B12), anti-MYC (9E11) or anti FLAG (M2) antibodies overnight at 4°C. Four mg of total protein extracts were incubated for 2 hours at 4°C. Input (IN) and IP RNAs were extracted using the Invitrogen Purelink RNA Mini and Micro Scale kits, respectively. DNase treatment, reverse transcription, and qPCR analyses of cDNA were performed as described for RT-qPCR analysis. IN samples were diluted 50-fold while IP samples were diluted 3-to-5-fold.

Relative binding levels were determined by dividing the IP by the IN value (IP/IN) for each amplicon. To determine the specificity of enrichment of the tagged protein, the corresponding untagged control samples were included in each RIP experiment. All primer sequences are listed in Table S5.

Affinity purification

Protein complexes were purified by the tandem affinity purification (TAP) method, as described previously (Helmlinger et al., 2008; Rigaut et al., 1999), with minor modifications. 1-4 l of exponentially growing cells were harvested, snap-frozen as individual droplets, and grinded in liquid nitrogen using a Freezer/Mill® (Spex SamplePrep). Protein extraction was performed in either WEB buffer or CHAPS-containing lysis buffer (CLB) buffer (50mM HEPES-NaOH pH 7.4, 300mM NaCl, 5mM CHAPS, 0.5mM DTT), supplemented with protease and phosphatase inhibitors. Following purifications, 10% of 2 mM EGTA eluates were concentrated and separated on 4%–20% gradient SDS-polyacrylamide Tris-glycine gels (Biorad). Total protein content was visualized by silver staining, using the SilverQuest kit. For quantitative mass spectrometry analyses, 90% of 2 mM EGTA eluates were precipitated with TCA and analyzed by mass spectrometry (MS). A downscaled version of the TAP procedure was used for standard co-immunoprecipitation followed by western blot analysis, as described in Laboucarié et al. (2017).

Mass spectrometry and data analysis

Dry TCA precipitates from TAP eluates were denatured, reduced and alkylated. Briefly, each sample was dissolved in 89 μL of TEAB 100 mM. One microliter of DTT 1 M was added and incubation was performed for 30 min at 60°C. A volume of 10 μL of IAA 0.5 M was added (incubation for 30 min in the dark). Enzymatic digestion was performed by addition of 1 μg trypsin in TEAB 100 mM and incubation overnight at 30°C. After completing the digestion step, peptides were purified and concentrated using OMIX Tips C18 reverse-phase resin (Agilent Technologies Inc.) according to the manufacturer's specifications. Peptides were dehydrated in a vacuum centrifuge.

Samples were resuspended in 9 μL formic acid (0.1%, buffer A) and 2 μL were loaded onto a 15 cm reversed phase column (75 mm inner diameter, Acclaim Pepmap 100® C18, Thermo Fisher Scientific) and separated with an Ultimate 3000 RSLC system (Thermo Fisher Scientific) coupled to a Q Exactive Plus (Thermo Fisher Scientific) via a nanoelectrospray source, using a 143-min gradient of 2 to 40% of buffer B (80% ACN, 0.1% formic acid) and a flow rate of 300 nl/min.

MS/MS analyses were performed in a data-dependent mode. Full scans (375 – 1,500 m/z) were acquired in the Orbitrap mass analyzer with a 70,000 resolution at 200 m/z. For the full scans, 3 × 106 ions were accumulated within a maximum injection time of 60 ms and detected in the Orbitrap analyzer. The twelve most intense ions with charge states ≥ 2 were sequentially isolated to a target value of 1×10^5 with a maximum injection time of 45 ms and fragmented by HCD (Higher-energy collisional dissociation) in the collision cell (normalized collision energy of 28%) and detected in the Orbitrap analyzer at 17,500 resolution. Raw spectra were processed using the MaxQuant environment (v.1.5.5.1) (Cox and Mann, 2008) and Andromeda for database search with label-free quantification (LFQ), match between runs and the iBAQ algorithm enabled (Cox et al., 2011). The MS/MS spectra were matched against the UniProt Reference proteome (Proteome ID UP000002485) of *S. pombe* (strain 972 / ATCC 24843) (Fission yeast) (release 2017_10; https://www.uniprot.org/) and 250 frequently observed contaminants as well as reversed sequences of all entries. Different release versions were used, depending on the date of analysis (Table S6). Enzyme specificity was set to trypsin/P, and the search included cysteine carbamidomethylation as a fixed modification and oxidation of methionine, and acetylation (protein N-term) and/or phosphorylation of Ser, Thr, Tyr residue (STY) as variable modifications. Up to two missed cleavages were allowed for protease digestion. FDR was set at 0.01 for peptides and proteins and the minimal peptide length at 7.

The relative abundance of proteins identified in each affinity purification was calculated as described in Smits et al., (2013). Briefly, label-free quantification (LFQ) intensity-based values were transformed to a base 2 logarithmic scale (Log2), to fit the data to a Gaussian distribution and enable the imputation of missing values. Normalized LFQ intensities were compared between replicates, using a 1% permutation-based false discovery rate (FDR) in a two-tailed Student's t test. The threshold for significance was set to 1 (fold change = 2), based on the FDR and the ratio between TAP and 'no TAP' samples. The relative abundance of subunits in each purification eluate was obtained by dividing the LFQ intensity of that interactor (prey) to the LFQ intensity of the TAP purified protein (bait).

RNA-seq and data analysis

All strains were done in triplicate. RNA was extracted from 50 mL of exponentially growing cells RNA using TRIzol reagent. DNA was removed by DNase I digestion, using the TURBO DNA-free kit and RNA was cleaned using the RNeasy Mini kit. Total RNA quality and concentration was determined using an Agilent Bioanalyzer. Transcripts were purified by polyA-tail selection. Stranded dual-indexed cDNA libraries were constructed using the Illumina TruSeq Stranded mRNA Library Prep kit. Library size distribution and concentration were determined using an Agilent Bioanalyzer. 48 libraries were sequenced in one lane of an Illumina HiSeq 4000, with 1x 50 bp single reads, at Fasteris SA (Plan-les-Ouates, Switzerland). After demultiplexing according to their index barcode, the total number of reads ranged from 6 to 10 million per library.

Adaptor sequences were trimmed from reads in the Fastq sequence files. Reads were aligned using HISAT2 (Kim et al., 2015), with strand-specific information (–rna-strandness R) and otherwise default options. For all 48 samples, the overall alignment rate was over 95%, including over 90% of reads mapping uniquely to the *S. pombe* genome. Reads were then counted for gene and exon features

using htseq-count (Anders et al., 2015) in union mode (–mode union), reverse stranded (–stranded Reverse), and a minimum alignment quality of 10 (–minaqual 10). For all samples, over 95% of reads were assigned to a feature (–type gene). Variance-mean dependence was estimated from count tables and tested for differential expression based on a negative binomial distribution, using DESeq2 (Love et al., 2014). Pairwise comparison or one-way analysis of variance were run with a parametric fit and genotype as the source of variation (factor: 'mutant' or 'control'). All computational analyses were run in R or Python.

QUANTIFICATION AND STATISTICAL ANALYSIS

All statistical tests were performed using RStudio (version 1.3.1056) and R (version 3.6.0) for RNA-seq data and GraphPad Prism (version 9.2.0) for proteomic data. All other experiments were analyzed using GraphPad Prism. t tests were used when comparing two means. Oneway or two-way analyses of variance (ANOVA) were performed for comparing more than two means, across one (for example ''genotype'') or two distinct variables (for example ''genotype'' as a between-subject factor and ''bait'' as a within-subject factor). One-way and two-way ANOVAs were followed by Tukey and Bonferroni post hoc pairwise comparisons, respectively. A significance level (α) of 0.01 was used *a priori* for all statistical tests, except otherwise indicated. Comparisons that are statistically significant ($p \leq 0.01$) are marked with one asterisk. Statistical details of experiments can be found in the figure legends, including the statistical tests used, the minimum value of biological replicates n shown (n = isogenic clones of each strain), and a description of the center and dispersion statistics shown. Quantitative values are typically represented as individual values (n) overlaid with the mean (black bar) and standard deviation (SD).

Cell Reports, Volume *37*

Supplemental information

The Hsp90 cochaperone TTT promotes cotranslational maturation of PIKKs prior to complex assembly

Damien Toullec, Alberto Elías-Villalobos, Céline Faux, Ambre Noly, Gwendaline Lledo, Martial Séveno, and Dominique Helmlinger

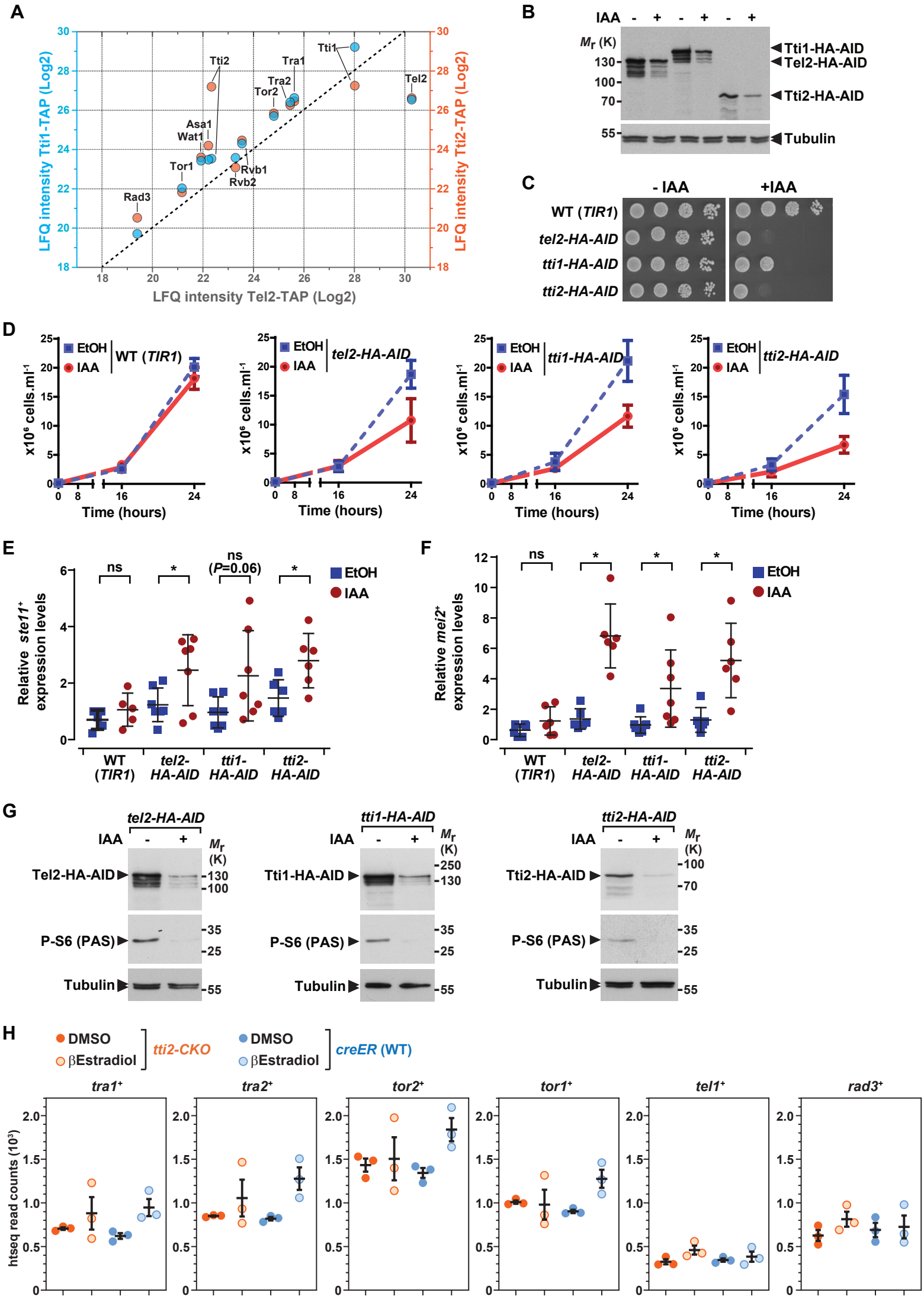
A
LFQ intensity Tti1-TAP (Log2)
LFQ intensity Tti2-TAP (Log2)
LFQ intensity Tel2-TAP (Log2)
Tti1
Tti2
Tra1
Tra2
Tor2
Tel2
Asa1
Wat1
Tor1
Rvb1
Rvb2
Rad3
B
IAA - + - + - +
Mr (K)
130
100
70
55
Tti1-HA-AID
Tel2-HA-AID
Tti2-HA-AID
Tubulin
C
- IAA
+IAA
WT (TIR1)
tel2-HA-AID
tti1-HA-AID
tti2-HA-AID
D
EtOH
IAA
WT (TIR1)
tel2-HA-AID
tti1-HA-AID
tti2-HA-AID
x10⁶ cells.ml⁻¹
Time (hours)
E
Relative ste11⁺ expression levels
ns
*
ns (P=0.06)
*
EtOH
IAA
WT (TIR1)
tel2-HA-AID
tti1-HA-AID
tti2-HA-AID
F
Relative mei2⁺ expression levels
ns
*
*
*
EtOH
IAA
WT (TIR1)
tel2-HA-AID
tti1-HA-AID
tti2-HA-AID
G
tel2-HA-AID
tti1-HA-AID
tti2-HA-AID
IAA - +
Mr (K)
Tel2-HA-AID
Tti1-HA-AID
Tti2-HA-AID
P-S6 (PAS)
Tubulin
130
100
250
70
35
25
55
H
DMSO
βEstradiol
tti2-CKO
creER (WT)
tra1⁺
tra2⁺
tor2⁺
tor1⁺
tel1⁺
rad3⁺
htseq read counts (10³)

Figure S1. Related to Figure 1. Biochemical and functional characterization of the *S. pombe* TTT complex.

(A) Mass spectrometry characterization of the TTT complex and its interacting partners in *S. pombe*. Comparative mass spectrometry analysis (LC-MS/MS) of tandem affinity purified Tel2, Tti1, and Tti2. Individual points represent label-free quantification (LFQ) intensities of interacting proteins enriched in each TAP eluates (n =1). Only proteins enriched at least 3-fold compared to a 'no TAP' control purification are shown. Each bait is depicted next to each axis. The blue-coloured y-axis allows comparing Tel2 with Tti1 eluates, whereas the red-coloured y-axis allows comparing Tel2 with Tti2 eluates. The black dashed line shows a 1:1 ratio.

(B-G) TTT controls PIKK-dependent processes.

(B) Western blot analysis of Tel2-, Tti1-, Tti2-HA-AID expression in strains grown to exponential phase in minimal medium supplemented with either ethanol (EtOH) or 0.5 mM auxin (IAA) for 16 hours. An anti-Tubulin antibody served as loading control.

(C,D) Viability and proliferation of *tel2-*, *tti1-* and *tti2-HA-AID* strains, cultured as in (B). (C) Ten-fold serial dilutions were spotted on corresponding solid media and grown for 4 days at 25°C. (D) Proliferation was estimated by counting at least 200 cells at the indicated time points. Shown are the mean and SD of 3 independent experiments (n = 3).

(E,F) Expression of *ste11+* (E) and *mei2+* (F) using quantitative RT–qPCR of RNA extracted from *tel2-*, *tti1-* and *tti2-HA-AID* strains, cultured as in (B). *act1+* served as internal control for normalization across samples. mRNA levels were normalized to one control (WT) strain grown in EtOH, which value was arbitrarily set to 1, to allow comparison between genotypes and culture conditions. Values from independent experiments are shown as individual points (n = 5), overlaid with the mean and SD. Statistical significance was calculated by unpaired *t*-tests (*$P < 0.05$).

(G) Western blot analysis of S6 protein phosphorylation (P-S6) in *tel2-*, *tti1-* and *tti2-HA-AID* strains, cultured as in (B), using anti-HA and anti-PAS antibodies. An anti-Tubulin antibody served as loading control.

(H) TTT does not affect PIKK mRNA levels. Analysis of *tra1+, tra2+, tor2+, tor1+, tel1+* and *rad3+* expression upon conditional knock-out of *tti2+*. mRNA levels were measured by extracting read counts from htseq analysis of RNA-seq. RNAs were extracted from *tti2-CKO* strains grown to exponential phase in rich medium supplemented with DMSO or 1 µM β-estradiol. *creER* (WT) strains were used as controls. Individual points represent the value from one experiment, overlaid with the mean and SD (n = 3).

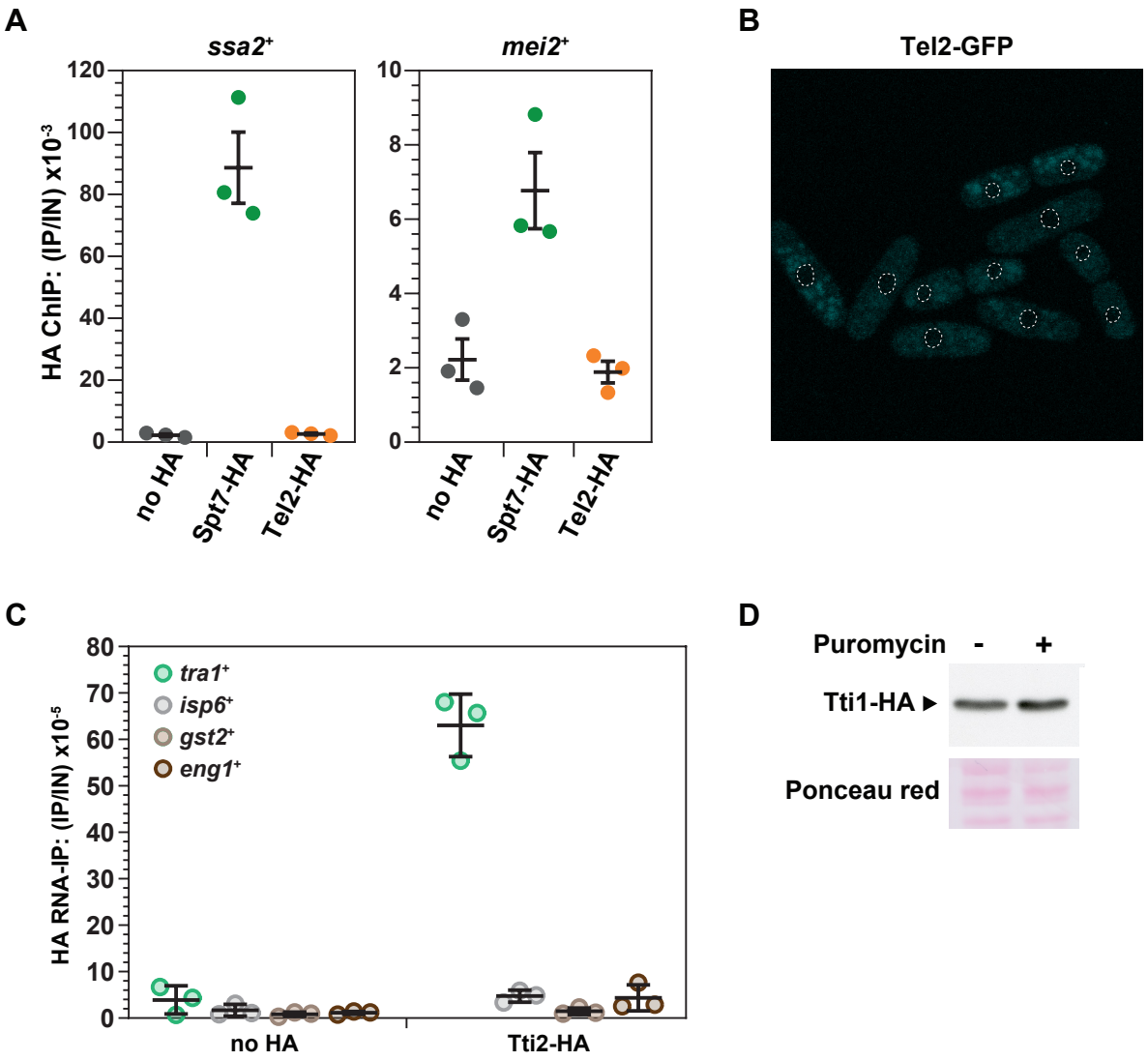

Figure S2. Related to Figure 2. Controls for TTT cotranslational interactions.

(A-B) The TTT subunit Tel2 does not localize to the nucleus in *S. pombe*.

(A) Tel2 is not detectable at Spt7-bound promoters. ChIP-qPCR analysis of Tel2-HA occupancy at the *ssa2*+ and *mei2*+ promoters. An Spt7-HA strain was used as a positive control. An untagged strain was used as control for background IP signal (no HA). Ratios of anti-HA ChIP to input (IP/IN) from three independent experiments are shown as individual points (n = 3), overlaid with the mean and SD.

(B) Tel2 is not detectable in the nucleus. Tel2-GFP localisation was assessed by live fluorescent microscopy of exponentially growing *S. pombe* cells. Nuclei were stained with DAPI and delimited with white dashed lines.

(C-D) Specificity of the cotranslational interaction between Tti2 and Tra1.

(C) Quantitative RT-PCR analysis of the *gst2*+ and *eng1*+ mRNAs Tti2 RIPs. Anti-HA IPs were performed using RNA extracted from cells grown to exponential phase. Ratios of IP to input (IP/IN) from independent experiments are shown as individual points (n = 3), overlaid with the mean and SD. Data for the *tra1*+ and *isp6*+ mRNAs are shown as a positive and a negative control, respectively and reused from Figure 2. An untagged strain was used as a control for background IP signal.

(D) Tti1 protein levels are not affected by puromycin treatment in conditions used for RIPs. Cultures were treated with 1 mg/ml puromycin for 15 minutes and total protein extracts were analyzed by Western blot with an antibody against the HA epitope. Ponceau red was used as loading control.

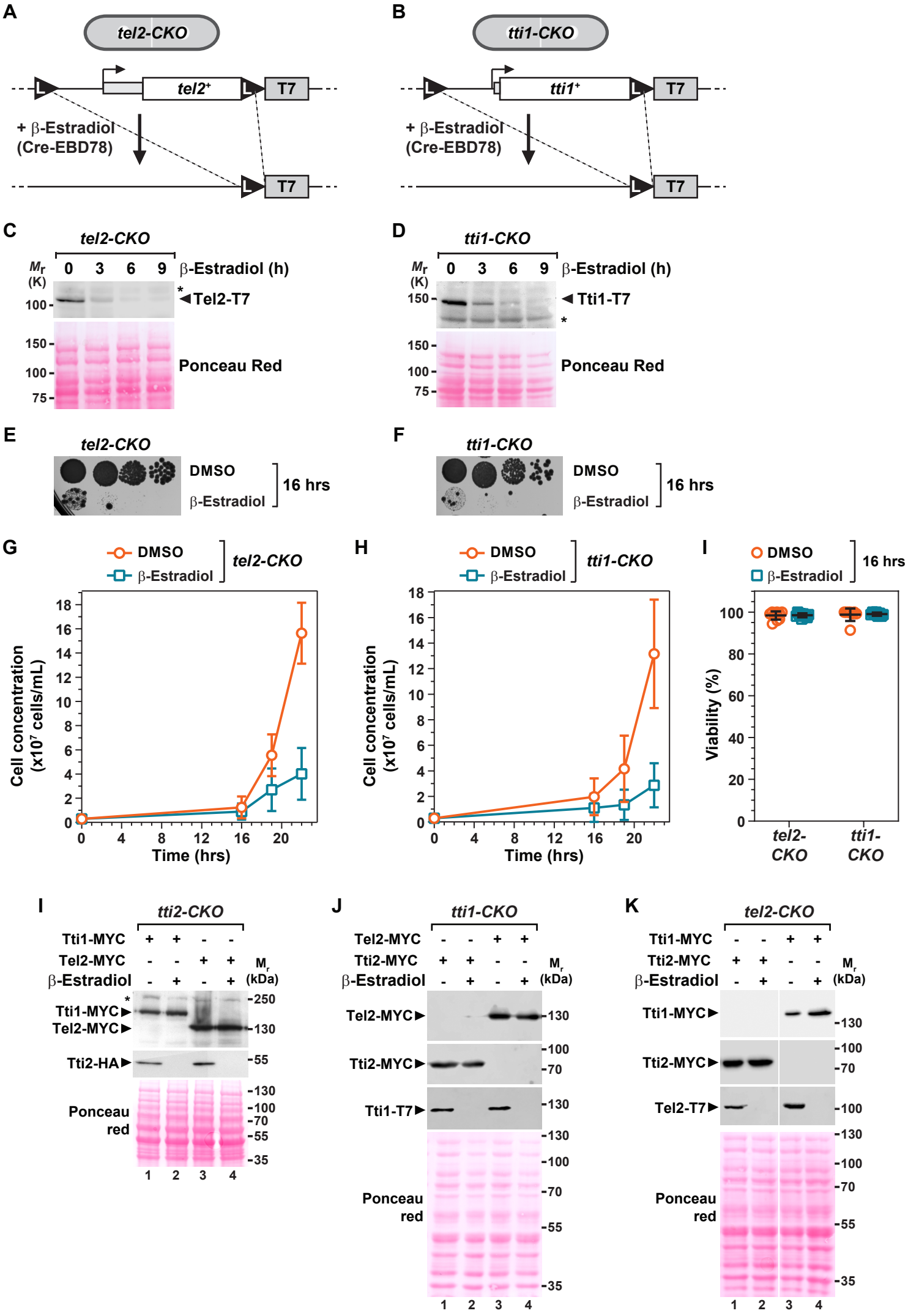
A
tel2-CKO
tel2+
T7
+ β-Estradiol
(Cre-EBD78)
T7
B
tti1-CKO
tti1+
T7
+ β-Estradiol
(Cre-EBD78)
T7
C
tel2-CKO
Mr (K)
0 3 6 9
β-Estradiol (h)
100
Tel2-T7
150
100
75
Ponceau Red
D
tti1-CKO
Mr (K)
0 3 6 9
β-Estradiol (h)
150
Tti1-T7
150
100
75
Ponceau Red
E
tel2-CKO
DMSO
β-Estradiol
16 hrs
F
tti1-CKO
DMSO
β-Estradiol
16 hrs
G
DMSO
β-Estradiol
tel2-CKO
Cell concentration (x10⁷ cells/mL)
Time (hrs)
H
DMSO
β-Estradiol
tti1-CKO
Cell concentration (x10⁷ cells/mL)
Time (hrs)
I
DMSO
β-Estradiol
16 hrs
Viability (%)
tel2-CKO
tti1-CKO
I
tti2-CKO
Tti1-MYC
Tel2-MYC
β-Estradiol
Mr (kDa)
Tti1-MYC
Tel2-MYC
Tti2-HA
Ponceau red
1 2 3 4
J
tti1-CKO
Tel2-MYC
Tti2-MYC
β-Estradiol
Mr (kDa)
Tel2-MYC
Tti2-MYC
Tti1-T7
Ponceau red
1 2 3 4
K
tel2-CKO
Tti1-MYC
Tti2-MYC
β-Estradiol
Mr (kDa)
Tti1-MYC
Tti2-MYC
Tel2-T7
Ponceau red
1 2 3 4

Figure S3. Related to Figure 2. Characterization of conditional TTT deletion mutants.

(A-I) CreER-mediated inducible knock-out of Tel2 and Tti1.

(A,B) Illustration of the *tel2+* (A) and *tti1+* (B) loci engineered with loxP sites (L black triangles) flanking the entire gene in the *tel2-CKO* and *tti1-CKO* strains, respectively, before and after induction of Cre recombinase with β-estradiol.

(C,D) Anti-T7 Western blot analyses of Tel2-T7 (E) and Tti1-T7 (F) expression at different time points upon *tel2+* and *tti1+* deletion, respectively. Ponceau red staining is used as a loading control. The star (*) symbol labels an unspecific band detected by the anti-T7 antibody in *S. pombe*.

(E,F) Estimation of recombination efficiency. Ten-fold serial dilutions of *tel2-CKO* (C) and *tti1-CKO* (D) cultures treated with either DMSO or β-estradiol for 16 hours were spotted on rich medium and incubated for 3 days at 32°C.

(G,H) Proliferation defects of *tel2-CKO* (G) and *tti1-CKO* (H) strains estimated from growth curves of yeasts growing exponentially in liquid culture, at different time points of DMSO and β-estradiol treatment (orange circles and blue squares, respectively). Each value represents the average number of cells from six independent replicates with the SD (n = 6). At least 100 cells were counted at each time point.

(I) Viability of of *tel2-CKO* and *tti1-CKO* strains grown in liquid media and treated with either DMSO (orange circles) or β-estradiol (blue squares) for 16 hours. The percentage of viable cells was estimated from methylene blue staining of liquid cultures and counting at least 100 cells by light microscopy. Six independent experiments are shown as individual points, overlaid with the mean and SD (n = 6).

(I-K) TTT subunit levels are not affected by the loss of TTT components.

(I) Anti-MYC Western blot analyses of Tti1-MYC (lanes 1-2) and Tel2-MYC (lanes 3-4) expression upon *tti2+* deletion (*tti2-CKO*), using *lox-tti2-lox-HA tti1-MYC* and *lox-tti2-lox-HA tel2-MYC* strains, respectively. Exponentially growing cells were treated with either DMSO or β-estradiol for 16 hours before protein extraction. An anti-HA antibody was used to confirm Tti2 deletion. Ponceau red staining is used as a loading control. The star (*) symbol labels an unspecific band detected by the anti-MYC antibody in *S. pombe*.

(J) Anti-MYC Western blot analyses of Tti2-MYC (lanes 1-2) and Tel2-MYC (lanes 3-4) expression upon *tti1+* deletion (*tti1-CKO*), using *lox-tti1-lox-T7 tti2-MYC* and *lox-tti1-lox-T7 tel2-MYC* strains, respectively. Exponentially growing cells were treated with either DMSO or β-estradiol for 16 hours before protein extraction. An anti-T7 antibody was used to confirm Tti1 deletion. Ponceau red staining is used as a loading control.

(K) Anti-MYC Western blot analyses of Tti2-MYC (lanes 1-2) and Tti1-MYC (lanes 3-4) expression upon *tel2+* deletion (*tel2-CKO*), using *lox-tel2-lox-T7 tti2-MYC* and *lox-tel2-lox-T7 tti1-MYC* strains, respectively. Exponentially growing cells were treated with either DMSO or β-estradiol for 16 hours before protein extraction. An anti-T7 antibody was used to confirm Tti1 deletion. Ponceau red staining is used as a loading control..

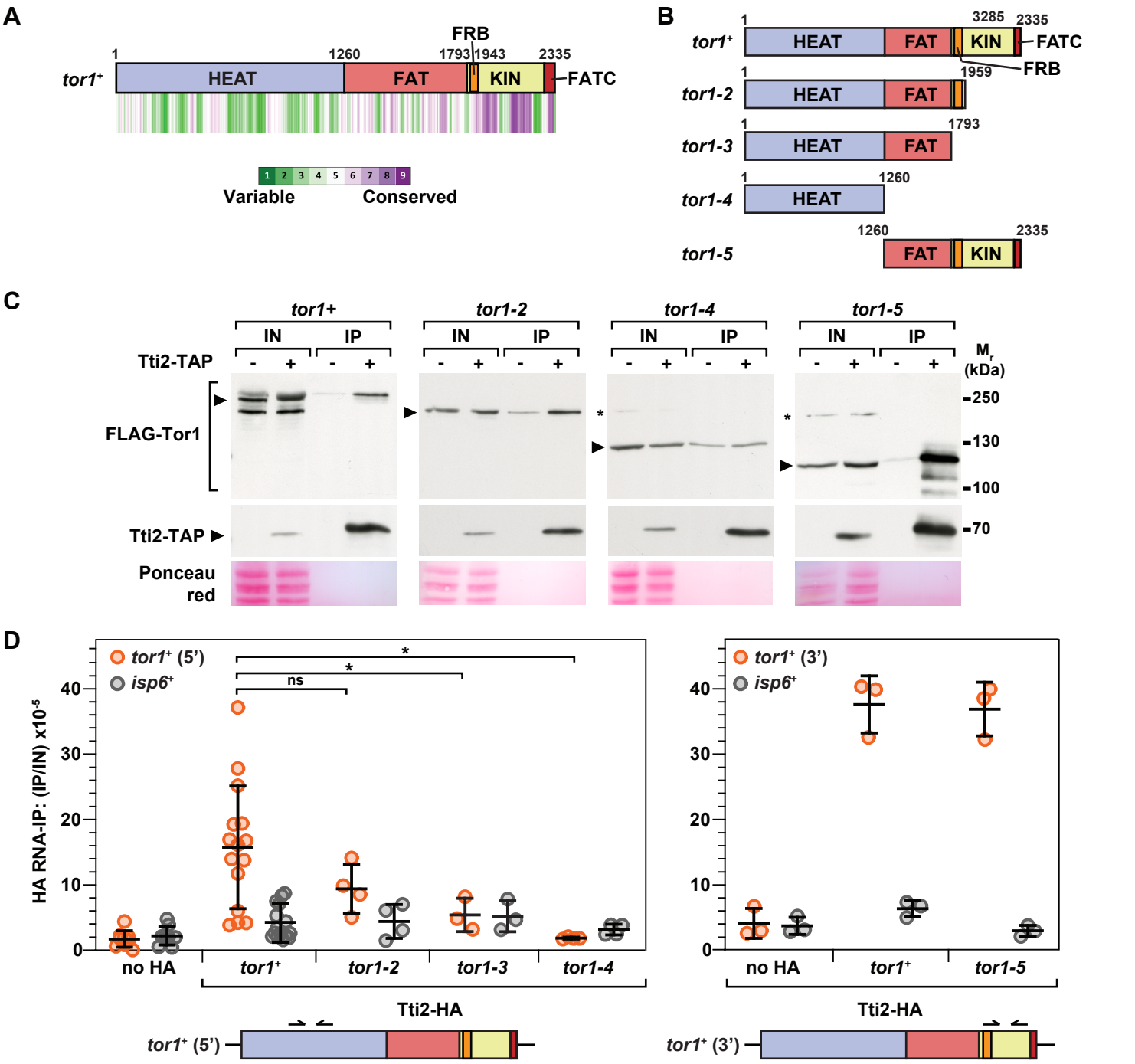

Figure S4. Related to Figure 3. Structure-function analysis of Tor1 interaction with TTT.

(A) Evolutionary conservation analysis from multiple sequence alignments of PIKKs from S. pombe. Conservation scores were calculated using ConSurf from multiple sequence alignments generated using Clustal Omega. Scores were averaged in 25-residue bins and shown as a heatmap, coloured as shown on the scale, and aligned to Tor1 domain organization (HEAT, FAT, FRB, KIN, and FATC).

(B) Schematic illustration of C- and N-terminal truncations of *S. pombe* Tor1. Truncations remove the KIN and FATC (*tor1-2*), the FRB, KIN, and FATC (*tor1-3*), the entire 'FATKIN' unit (*tor1-4*), or the HEAT repeats (*tor1-5*). The first and last residues of each truncated mutant protein are shown.

(C) Western blot analysis of Tor1 binding to TTT in Tti2-TAP IPs from a wild-type (WT) FLAG-Tor1 strain and FLAG-Tor1 truncation mutants. An untagged strain is used as a control for IPs. IPs and inputs were analysed by Western blot with antibodies against FLAG and TAP epitope. Ponceau red was used as loading control for the inputs. The star (*) symbol labels an unspecific band detected by the anti-FLAG antibody in *S. pombe*.

(D) RIP-qPCR analysis of *tor1* mRNAs in Tti2-HA IPs from WT and mutant alleles of *tor1+*. Anti-HA IPs were performed using RNA extracted from cells grown to exponential phase. Ratios of IP to input (IP/IN) from independent experiments are shown as individual points (n ≥ 3), overlaid with the mean and SD. The *isp6+* mRNA is used as a negative control. An untagged strain is used as a control for background signal. The bottom diagram shows the position of the primers used for *tor1+* qPCR. Statistical significance was determined by one-way ANOVA followed by Tukey's multiple comparison tests (asterisk: $P < 0.05$).

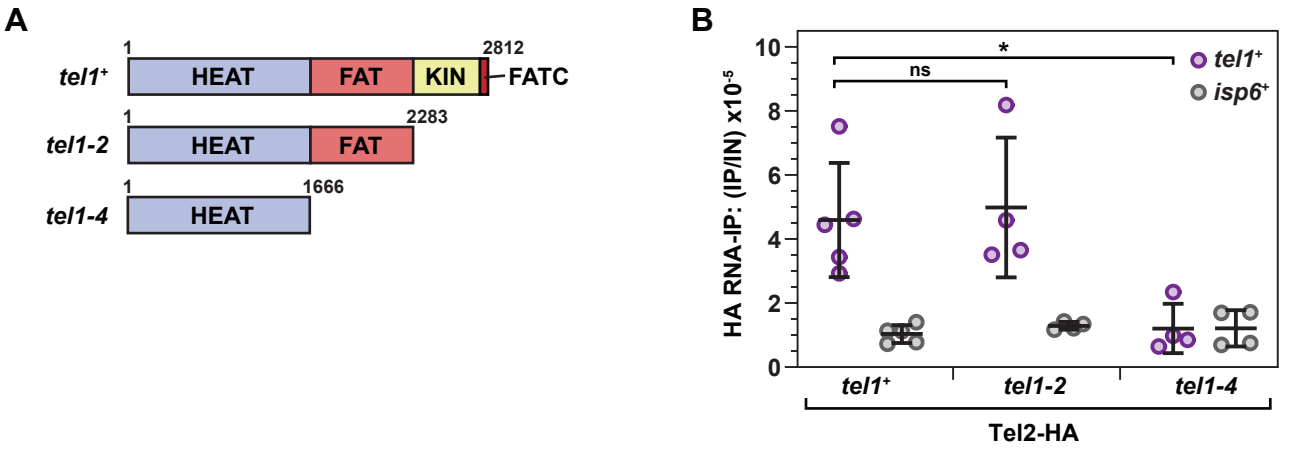

Figure S5. Related to Figure 3. Structure-function analysis of Tel1 interaction with TTT.

(A) Schematic illustration of C- and N-terminal truncations of *S. pombe* Tel1. Truncations remove the KIN and FATC (*tel1-2*) or the FAT, KIN, and FATC domains (*tel1-4*). Mutant alleles are numbered according to the nomenclature used for naming *tra1* and *tor1* mutant alleles in Figure 4 and S8. The first and last residues of each truncated mutant protein are shown.

(B) RIP-qPCR analysis of *tel1* mRNAs in Tel2-HA IPs from WT and mutant alleles of *tel1+*. Anti-HA IPs were performed using RNA extracted from cells grown to exponential phase. Ratios of IP to input (IP/IN) from independent experiments are shown as individual points, overlaid with the mean and SD. The *isp6+* mRNA is used as negative control. Statistical significance was determined by one-way ANOVA followed by Tukey's multiple comparison tests (asterisk: $P < 0.05$).

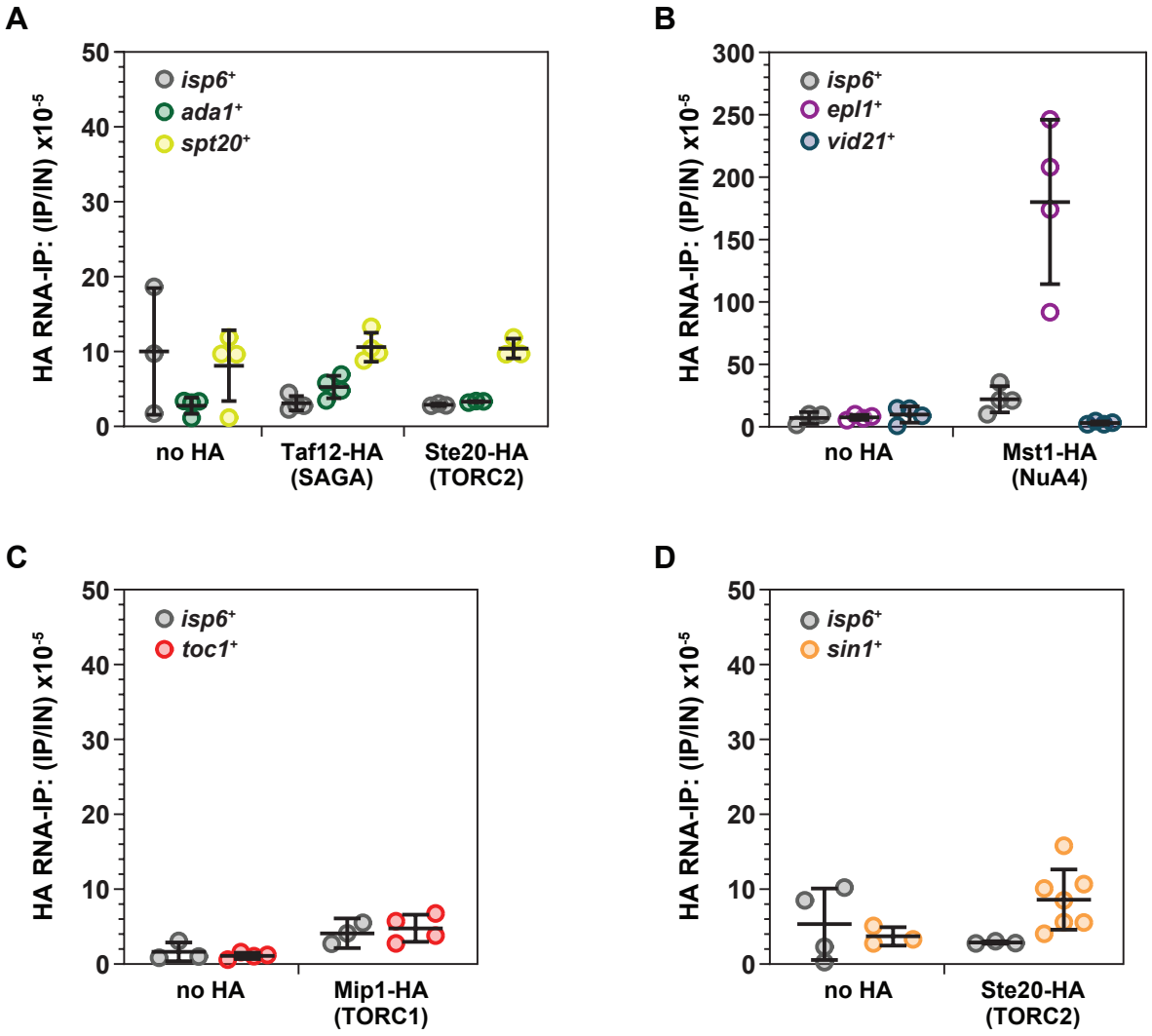

Figure S6. Related to Figure 5. Cotranslational interactions between SAGA, NuA4, TORC1, and TORC2 subunits.

(A-D) Quantitative RT-PCR analysis of the indicated mRNAs in RIPs of SAGA, NuA4, TORC1, and TORC2 subunits. Anti-HA IPs were performed using RNA extracted from cells grown to exponential phase. Ratios of IP to input (IP/IN) from independent experiments are shown as individual points (n ≥ 3), overlaid with the mean and SD. Data for the *isp6*$^{+}$ mRNA iare shown as a negative control and reused from Figure 6. An untagged strain was used as a control for background IP signal.

(A) *ada1*$^{+}$ and *spt20*$^{+}$ mRNA levels in Taf12-HA and Ste20-HA IPs.

(B) *epl1*$^{+}$ and *vid21*$^{+}$ mRNA levels in Mst1-HA IPs.

(C) *toc1*$^{+}$ mRNA levels in Mip1-HA IPs.

(D) *sin1*$^{+}$ mRNA levels in Ste20-HA IPs.

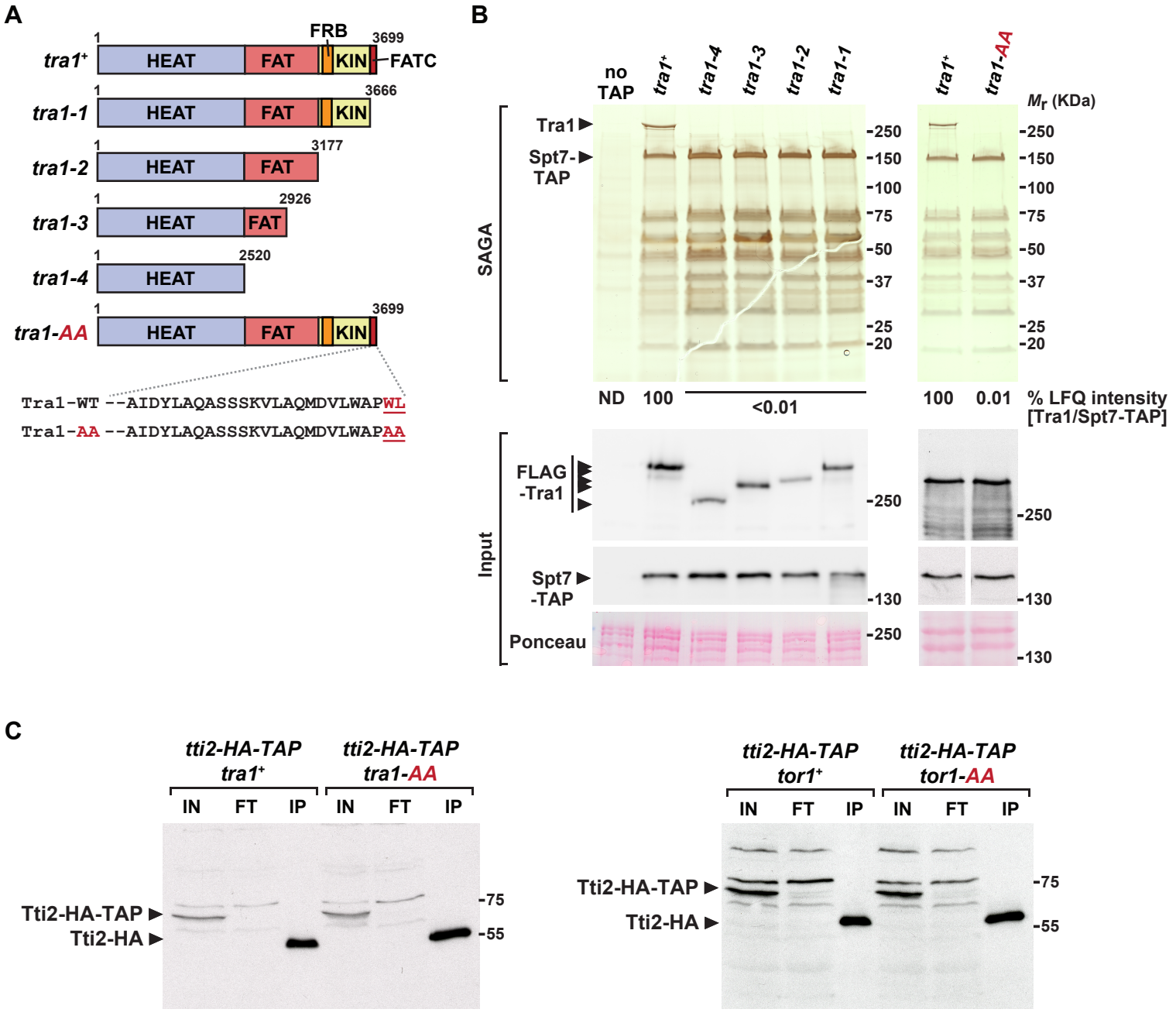

Figure S7. Related to Figure 6. Structure-function analysis of Tra1 interaction with SAGA.

(A) Schematic illustration of C-terminal truncation and point mutant alleles of *S. pombe tra1+*. Distinct colours depict the Tra1 domains: HEAT, FAT, KIN, and FATC. Truncation mutations remove the FATC (*tra1-1*), the KIN and the FATC (*tra1-2*), half of the FAT, KIN and FATC (*tra1-3*), or the entire FAT, KIN and FATC domains (*tra1-4*). The last residue of each truncated mutant protein is shown. The *tra1-AA* allele was constructed by substituting the last two residues with alanines.

(B) Silver staining of SAGA complexes purified from a WT strain and different *tra1* mutants, using Spt7 as the bait. An untagged strain (no TAP) was used as a control for background. Numbers at the bottom of the gel represent LFQ intensity ratios of Tra1 to Spt7, from LC-MS/MS analyses of purified SAGA complexes. Values for each mutant are expressed as percentage of WT SAGA. Shown are gels that are representative of three independent experiments (n =3). Below are anti-FLAG anti-HA Western blots of FLAG-Tra1 and Spt7-HA-TAP in a fraction of the input used for tandem affinity purifications.

(C) Related to Figure 7. Western blot controls for TAPs of TTT in Tra1 and Tor1 FATC mutants. Anti-HA Western blot analyses of Tti2-TAP in a fraction of the input used for the TAPs shown in Figure 7A,B. Fractions of the flow through from the IgG column (FT) and the final EGTA eluate (IP) were also analyzed.

Table S3. Related to Figure 3. Quantification of Western blot signal intensities of FLAG-Tra1 and Tti2-TAP in input and IP fractions. Ratios of IP to input (IP/IN) from two independent experiments (n = 2) were averaged and normalized to the ratios obtained in coIPs of WT Tra1.

IP/input	*tra1 +*	*tra1-1*	*tra1-2*	*tra1-4*	*tra1-5*	*tra1-6*
FLAG-Tra1	1.0	0.5	0.0	0.0	0.8	0.0
Tti2-TAP	1.0	3.6	4.2	2.8	10.6	21.7